

Dynamics of $A + B \rightarrow C$ reaction fronts under radial advection in a Poiseuille flowAlessandro Comolli , A. De Wit , and Fabian Brau **Université libre de Bruxelles (ULB), Nonlinear Physical Chemistry Unit, CP231, 1050 Bruxelles, Belgium*

(Received 7 July 2021; accepted 24 September 2021; published 18 October 2021)

$A + B \rightarrow C$ reaction fronts describe a wide variety of natural and engineered dynamics, according to the specific nature of reactants and product. Recent works have shown that the properties of such reaction fronts depend on the system geometry, by focusing on one-dimensional plug flow radial injection. Here, we extend the theoretical formulation to radial deformation in two-dimensional systems. Specifically, we study the effect of a Poiseuille advective velocity profile on $A + B \rightarrow C$ fronts when A is injected radially into B at a constant flow rate in a confined axisymmetric system consisting of two parallel impermeable plates separated by a thin gap. We analyze the front dynamics by computing the temporal evolution of the average over the gap of the front position, the maximum production rate, and the front width. We further quantify the effects of the nonuniform flow on the total amount of product, as well as on its radial concentration profile. Through analytical and numerical analyses, we identify three distinct temporal regimes, namely (i) the early-time regime where the front dynamics is independent of the reaction, (ii) the transient regime where the front properties result from the interplay of reaction, diffusion that smooths the concentration gradients and advection, which stretches the spatial distribution of the chemicals, and (iii) the long-time regime where Taylor dispersion occurs and the system becomes equivalent to the one-dimensional plug flow case.

DOI: [10.1103/PhysRevE.104.044206](https://doi.org/10.1103/PhysRevE.104.044206)**I. INTRODUCTION**

Reaction-diffusion (RD) fronts are observed in a broad variety of natural and engineered systems, e.g., in population dynamics [1], disease spreading [2–4], biological pattern formation [5], transport of ions in cells [6], nonlinear phenomena in physics [7], combustion [8], finance [9], and more. $A + B \rightarrow C$ fronts are an important subset of RD fronts. They develop when the reactants A and B , initially spatially separated, are transported through diffusion and react to form the product C . Depending on the specific nature of A , B , and C , this class of fronts is found in several problems in geochemistry [10], catalysis [11], atmospheric chemistry [12], and ecological [13] and environmental problems [14], to name a few.

So far, the dynamics of $A + B \rightarrow C$ fronts has typically been studied theoretically for simple one-dimensional (1D) geometries, that is, by assuming invariance in the other two spatial dimensions. Gálfi and Rácz [15] paved the way to the study of $A + B \rightarrow C$ reaction-diffusion fronts in the 1D rectilinear geometry, where the initial contact zone between the reactants is planar and the reactants are transported only through molecular diffusion. Their theoretical predictions on the evolution of the front position and shape have meanwhile found numerical [16] and experimental [17,18] confirmation.

Recently, the case of radial reaction-diffusion-advection (RDA) $A + B \rightarrow C$ fronts has started to be analyzed due to their ubiquity in a large variety of systems, including, e.g., infectious disease propagation on complex networks [19],

reactions on droplets [20], Liesegang rings [21,22], CO_2 mineralization in soils [23], or material synthesis in nonequilibrium conditions [24–27], to cite a few. Specifically, theoretical analysis of the front dynamics has started to be tackled in the case of 1D radial symmetry with diffusive transport [21,22,28]. Advected fronts developing when A is injected radially at a constant flow rate into B in systems with polar [29–31] or spherical [32] symmetry have further been addressed.

The 1D polar theory [29,30] assumes that the equations that govern the front dynamics depend on the radial coordinate only. When transport and reaction occur in a volume delimited by two parallel plates, this is equivalent to assuming a plug flow. However, experiments that were carried out in Hele-Shaw cells [29,33] show that the 1D plug flow model underestimates the measured amount of product, as it does not account for enhanced transverse mixing. The authors suggest that this discrepancy can be traced back to the heterogeneity of the velocity field across the gap, which cannot be embraced by 1D models. Several experimental [34,35] and theoretical [36–38] studies have tackled the problem of $A + B \rightarrow C$ dynamics in Poiseuille flows, as a base example of microscale reactive transport processes in porous or fractured media. However, these works considered either a rectilinear injection of A into B [34] or a relaxation of a reaction-diffusion front in a radial geometry after stopping the injection of A into B when reaching a given radius [35]. In the radial advective geometry, the velocity field depends both on the distance from the plates in the gap and on the radial distance from the inlet. Understanding the impact of such nonuniform velocities on the dynamics of the reactive fronts remains an open problem.

*fabian.brau@ulb.be

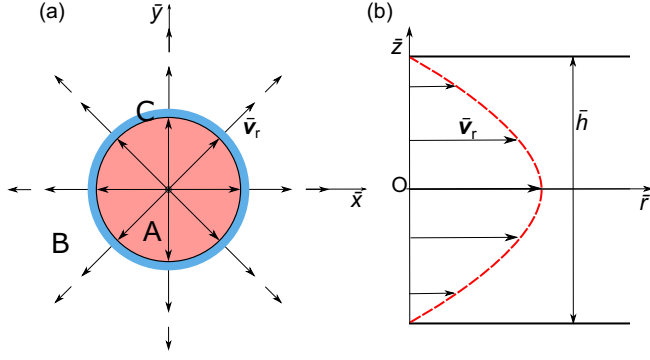


FIG. 1. Schematic illustration of the system. (a) Top view showing in the (\bar{x}, \bar{y}) plane the reactant A injected radially with a velocity $\bar{v}_r(\bar{r}, \bar{z})$ into the reactant B. The product C is generated in the miscible contact zone between the reactants. (b) Lateral view of the velocity field, showing the Poiseuille profile in the (\bar{r}, \bar{z}) coordinate system.

In this context, we study theoretically the properties of radial $A + B \rightarrow C$ reaction-diffusion-advection fronts in a 2D axisymmetric confined geometry when the laminar injection generates a Poiseuille velocity field $\bar{v}_r(\bar{r}, \bar{z})$; see Fig. 1. The reactant A is injected into B at a constant flow rate \bar{Q} and all the species have the same mobility properties. The Poiseuille flow deforms the reaction front in the gap of the reactor as reactants and products are initially transported at different velocities, depending on their position along the gap. As a result, the curvature of the front and its length increase due to advective stretching. At later times, this effect is contrasted by transverse diffusion along the gap, which makes reactants and product move across the flow lines. Then, the system evolves toward a Taylor dispersion regime, where the dependence on \bar{z} is lost and the dynamics is conveniently described by the radial 1D theory. We study the temporal evolution of the front characteristics, namely its position, the maximum of the production rate, and its width across these three successive regimes. We characterize them analytically and numerically in terms of their respective temporal scalings.

This paper is structured as follows. Section II introduces the model and its nondimensionalization and presents the relevant timescales and the observables that are analyzed throughout the paper. Section III describes the front dynamics. In Sec. IV, we study the long-time regime, whereas the preasymptotic dynamics is analyzed in Sec. V. Finally, Sec. VI summarizes the key findings and concludes the paper.

II. MODEL

We consider a 2-dimensional axisymmetric system confined by two impermeable plates located at $\bar{z} = \pm\bar{h}/2$, where \bar{z} is the coordinate along the vertical axis; see Fig. 1. The system conveniently describes, for instance, the geometry of a Hele-Shaw cell. This reactor is initially filled by a reactant B in dimensional concentration \bar{b}_0 . A reactant A in initial concentration \bar{a}_0 is injected radially into the cell from a point source located at the center of the system at a constant flow rate \bar{Q} . The product C is created by the irreversible $A + B \rightarrow C$ reaction upon contact of the reactants. All the species are transported by passive advection and diffusion. Their

dynamics is governed by the following set of coupled dimensional partial differential equations (PDEs),

$$\partial_{\bar{t}}\bar{a} + (\bar{v} \cdot \bar{\nabla})\bar{a} = D_a \bar{\nabla}^2 \bar{a} - k\bar{a}\bar{b}, \quad (1a)$$

$$\partial_{\bar{t}}\bar{b} + (\bar{v} \cdot \bar{\nabla})\bar{b} = D_b \bar{\nabla}^2 \bar{b} - k\bar{a}\bar{b}, \quad (1b)$$

$$\partial_{\bar{t}}\bar{c} + (\bar{v} \cdot \bar{\nabla})\bar{c} = D_c \bar{\nabla}^2 \bar{c} + k\bar{a}\bar{b}, \quad (1c)$$

where \bar{a} , \bar{b} , and \bar{c} are the dimensional concentrations of the corresponding species, D_a , D_b , and D_c are their diffusion coefficients, k is the kinetic constant of the reaction, \bar{v} is the advective velocity, and \bar{t} is the dimensional time. Throughout this paper, all dimensional quantities, except the diffusion coefficients and k , are denoted by an overline. For the sake of simplicity, we assume that all species share the same mobility properties by considering the same diffusion coefficient, namely $D = D_a = D_b = D_c$. Flow incompressibility, i.e., $\bar{\nabla} \cdot \bar{v} = 0$, and radial symmetry are assumed. Therefore, the only nonzero component of the velocity field is the radial component, i.e., $\bar{v} = \bar{v}_r(\bar{r}, \bar{z})\mathbf{e}_r$, where \mathbf{e}_r is the unit radial vector. Specifically, \bar{v} defines a Poiseuille flow along the radial direction with

$$\bar{v}_r(\bar{r}, \bar{z}) = \bar{v}_m(\bar{r}) \left(1 - \frac{4\bar{z}^2}{\bar{h}^2}\right), \quad \bar{v}_m(\bar{r}) = \frac{3\bar{Q}}{4\pi\bar{h}\bar{r}}, \quad (2)$$

where $\bar{v}_m(\bar{r})$ is the maximum velocity of the flow located at $\bar{z} = 0$ [39,40].

Dimensionless system

The nondimensionalization of the governing equations is carried out by rescaling time by $\tau = 1/k\bar{a}_0$ and space by $\ell = \sqrt{D\tau}$. In addition, all concentrations are rescaled by the initial concentration \bar{a}_0 of the injected reactant. Thus, the initial dimensionless concentration of the reactant B is given by $\gamma = \bar{b}_0/\bar{a}_0$. The dimensionless governing equations are derived from (1) and read

$$\partial_t a + (v_r - 1/r)\partial_r a = \partial_r^2 a + \partial_z^2 a - ab, \quad (3a)$$

$$\partial_t b + (v_r - 1/r)\partial_r b = \partial_r^2 b + \partial_z^2 b - ab, \quad (3b)$$

$$\partial_t c + (v_r - 1/r)\partial_r c = \partial_r^2 c + \partial_z^2 c + ab, \quad (3c)$$

where t , r , and z are the dimensionless time, radial, and vertical coordinates, respectively, and v_r is the radial dimensionless velocity

$$v_r(r, z) = \frac{3Q}{2r} \left(1 - \frac{4z^2}{h^2}\right), \quad Q = \frac{\bar{Q}}{2\pi\bar{h}D}, \quad (4)$$

where $h = \bar{h}/\ell$ is the dimensionless aperture gap. We solve the coupled PDEs (3) numerically with the initial conditions $a(r > 0, z, 0) = b(r \rightarrow 0, z, 0) = c(r, z, 0) = 0$, $a(r \rightarrow 0, z, 0) = 1$, and $b(r > 0, z, 0) = \gamma$, while the boundary conditions are $a(r \rightarrow 0, z, t) = 1$, $a(r \rightarrow \infty, z, t) = b(r \rightarrow 0, z, t) = c(r \rightarrow 0, z, t) = c(r \rightarrow \infty, z, t) = \partial_z a(r, z = \pm h/2, t) = \partial_z b(r, z = \pm h/2, t) = \partial_z c(r, z = \pm h/2, t) = 0$, and $b(r \rightarrow \infty, z, t) = \gamma$. The three parameters that control the system are the nondimensional flow rate Q , the nondimensional gap height h , and the ratio γ between the initial concentrations of B and A. The numerical computations are carried out through an in-house 2D solver written in C and based on the forward time centered space (FTCS) scheme.

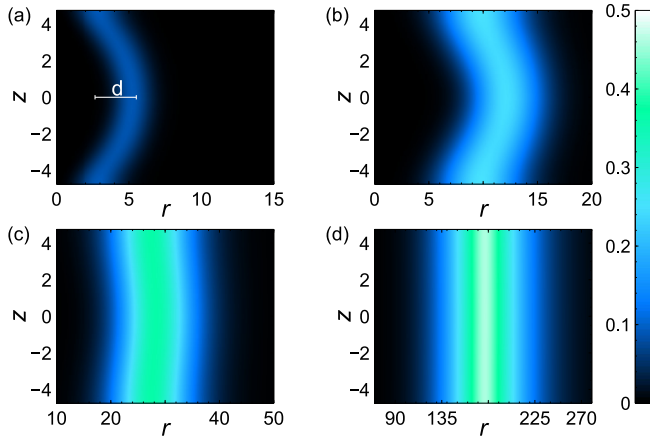


FIG. 2. Concentration $c(r, z)$ at times (a) $t = 1$, (b) $t = 6$, (c) $t = 40$, and (d) $t = 1585$ for $Q = 10$, $\gamma = 1$, and $h = 10$. The segment in panel (a) shows the distance $d = \tilde{r}_c(z = h/2) - \tilde{r}_c(z = 0)$.

The mesh is composed of $N_r \times N_z$ nodes, with $N_z = h/\Delta z$ and $N_r = L/\Delta r$. For the computations shown in this paper, the radial domain size L varies in the range 500–2500 and it increases for increasing Q , while the spatial discretization steps are $\Delta r = \Delta z = 0.1$ and the temporal integration step Δt is chosen according to the configuration to ensure convergence. Average quantities across the gap are computed as the arithmetic mean over the nodes with the same radial index.

III. FRONT DYNAMICS

The dynamics of the reaction front is illustrated in Fig. 2 through snapshots of the product concentration at different times. Reactant A is injected into B as a line at $r = 0$. By effect of the Poiseuille flow, which transports the reactants at a different velocity according to their position along z , the initially rectilinear interface along z is deformed along the curved shape shown in Fig. 2(a). Both the reactants and the product also diffuse across the gap exploring different flow lines. At longer times all reactants have equally experienced all the velocity variability within the gap. Therefore, the concentration distribution becomes homogeneous across the gap; see Fig. 2(d). This effect was first studied by Taylor [41] for conservative transport in a channel, and it is therefore known as Taylor dispersion. Some authors have generalized this process to reactive transport [38,42] in a channel. Here, we show that Taylor dispersion also arises when A is injected radially into B . We quantify this process through the temporal evolution of the curvature $\Omega(t) = d(t)/h^2$, shown in Fig. 3, where $d(t) = \tilde{r}_c(z = h/2, t) - \tilde{r}_c(z = 0, t)$, see Fig. 2(a), and \tilde{r}_c is the radial position at which the concentration of C at a given z is maximum. We observe that the curvature grows as $t^{1/2}$ in the early-time regime, it reaches a maximum, and then decreases as $t^{-1/2}$ in the long-time limit. In this asymptotic limit, the homogeneity along the gap allows us to treat the advective transport as that of a plug flow, i.e., to consider a 1D system with radial symmetry such as in [29,30].

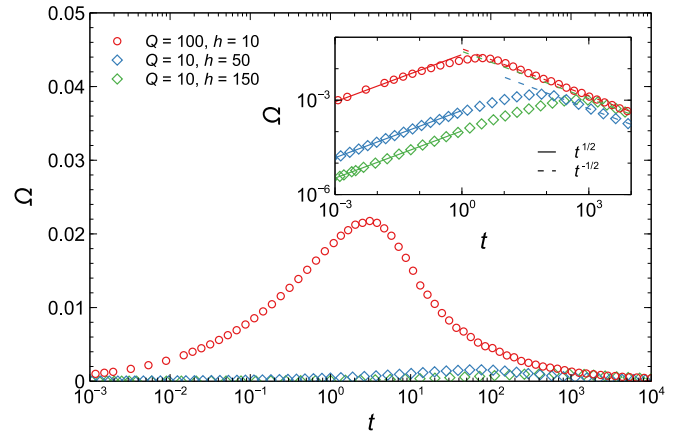


FIG. 3. Temporal evolution of the curvature Ω of the concentration profile of C for $\gamma = 1$ and various Q and h . Inset: Log-log plot.

Observables

To characterize the dynamics of $A + B \rightarrow C$ reaction fronts in the described system, we study the temporal evolution of observables averaged over the aperture gap, i.e., along the z direction. For a generic function $f(z)$, the average over the gap is defined as

$$\langle f \rangle = \frac{1}{h} \int_{-h/2}^{h/2} f(z) dz. \quad (5)$$

First, we introduce the radial position of the front, $r_f(t)$, which is classically defined as the position where the concentrations of A and B are equal [15,43],

$$\langle a \rangle(r_f, t) = \langle b \rangle(r_f, t). \quad (6)$$

In this work, we also consider a different definition of the front position, which can be of more practical use in experimental setups. In reaction-diffusion-advection experiments carried out in a Hele-Shaw cell [29,33,35], the concentration profile of the product C is indeed typically the only visible variable that can be quantified. Hence, it is convenient to introduce the radial front position r_c as the radial distance from the inlet where the average concentration $\langle c \rangle$ is maximum,

$$c_{\max}(t) = \max_r (\langle c \rangle(r, t)), \quad \langle c \rangle(r_c, t) = c_{\max}(t). \quad (7)$$

The average over the gap of the dimensionless production rate can be performed in two ways, either by multiplying the average of the concentrations or by averaging the product of the concentrations of A and B , i.e.,

$$R(r, t) = \langle a \rangle \langle b \rangle, \quad \tilde{R}(r, t) = \langle ab \rangle. \quad (8)$$

The maximum values of these quantities along the radial direction r are denoted with R^{\max} and \tilde{R}^{\max} , respectively.

The size of the front can be quantified through the radial width of the production rate or the width of the radial concentration profile of C . Specifically, let w , \tilde{w} , and w_c be the width at half height of R , \tilde{R} , and $\langle c \rangle$, respectively. The quantities introduced in this section are shown in Fig. 4. Finally, the total amount of product is obtained by integrating the concentration

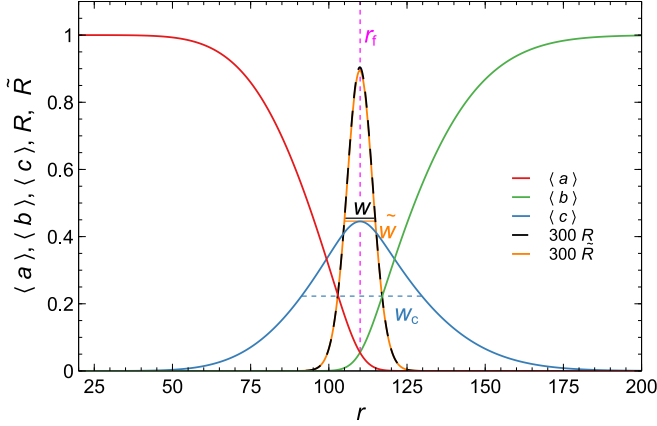


FIG. 4. Radial averaged concentration profiles and production rates computed at $t = 630$ for the following set of parameters: $Q = 10$, $\gamma = 1$, and $h = 20$.

of the product C over the entire domain,

$$n_c(t) = 2\pi \int_{-h/2}^{h/2} dz \int_0^\infty rc(r, z, t) dr, \quad (9)$$

where 2π accounts for the azimuthal integration, due to cylindrical symmetry. The dynamics of RDA fronts is characterized by three distinct temporal regimes, namely (i) the early-time (diffusion) regime, (ii) the transient (Poiseuille) regime, and (iii) the long-time (dispersion or Taylor) regime. In the following, each regime is described in terms of the temporal scalings of the observables presented in this section.

IV. LONG-TIME FRONT DYNAMICS

Figure 2(d) shows that, at long times, the concentrations are homogeneous along the gap. The system is thus equivalent to the 1D case of a plug flow for which scalings in radial flows have been recently derived [29]. We start the analysis of such RDA fronts by studying the asymptotic limit $t \rightarrow \infty$, in analogy with the studies on polar [29] and spherical [32] geometry. The early-time limit and the transient regime, which are affected by the Poiseuille profile, are studied subsequently. In the limit of large t , the temporal evolution of the z -averaged concentrations can be described in terms of the following set of approximated equations,

$$\partial_t a + \frac{Q-1}{r} \partial_r a - \partial_r^2 a + ab = E \left[\partial_r^2 a - \frac{1}{r} \partial_r a \right], \quad (10a)$$

$$\partial_t b + \frac{Q-1}{r} \partial_r b - \partial_r^2 b + ab = E \left[\partial_r^2 b - \frac{1}{r} \partial_r b \right], \quad (10b)$$

$$\partial_t c + \frac{Q-1}{r} \partial_r c - \partial_r^2 c - ab = E \left[\partial_r^2 c - \frac{1}{r} \partial_r c \right], \quad (10c)$$

where $E = Q^2 h^2 / 210 r^2$ and we have dropped the average signs for shortness. These equations are derived in Appendix A by assuming small initial concentrations \bar{a}_0 and shallow gap height \bar{h} . However, as we show in Fig. 5, the set of equations (10) approximates well the system dynamics even when the conditions for which these equations are derived are relaxed. Notice that when the front has traveled a distance

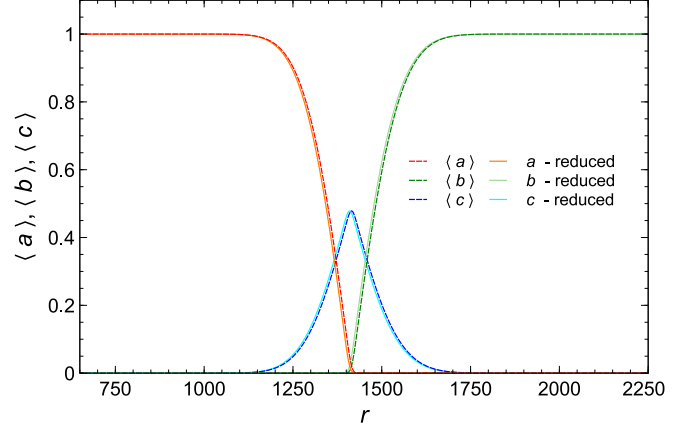


FIG. 5. Comparison between the average concentrations computed by solving numerically the full (3) and the approximated model (10) for $Q = 100$, $h = 26$, $\gamma = 1$ at $t = 10^4$.

$r \gg \sqrt{210} Q h$, the terms on the right-hand side of Eqs. (10) become negligible and we retrieve the same set of equations that describes the front dynamics for the $A + B \rightarrow C$ reaction in 1D when the reactants and the products undergo diffusion and passive radial advection [29]. This means that far from the injection point, the system reaches a dispersive regime in which the properties of the front do not depend on the position z along the gap. This is analogous to Taylor dispersion [41], which holds for conservative tracer transport in Poiseuille flows.

A. Front position

In the long-time dispersive regime, the behavior of the observables is the one derived for 1D radial injection in [29]. The asymptotic long-time front position $r_{f,A}$ is given by

$$r_{f,A}(t) = 2\sqrt{\mathcal{K}t} \quad \text{with} \quad \mathcal{K} = Q^{-1} \left(\frac{Q}{2}, \frac{\gamma}{1+\gamma} \right), \quad (11)$$

where the index A stands for asymptotic long time and $Q^{-1}(\alpha, x)$ is the unique solution for $y \geq 0$ with $0 \leq x \leq 1$ and $\alpha > 0$ of the equation $x = Q(\alpha, y)$, where $Q = \Gamma(\alpha, x) / \Gamma(\alpha)$, $\Gamma(\alpha, x)$, and $\Gamma(\alpha)$ are the regularized, incomplete, and complete gamma functions, respectively [44]. Notice that for $Q \gg 1$ and $\gamma \simeq 1$, Eq. (11) reduces to [29]

$$r_{f,A}(t) \simeq 2\sqrt{t} \left(\frac{Q}{2} + \frac{1-\gamma}{1+\gamma} \frac{\sqrt{\pi Q}}{2} \right)^{1/2}. \quad (12)$$

As shown in Fig. 6, Eq. (11) is in good agreement with the results obtained from numerical solutions of Eq. (3). Notice that for fixed values of h and γ , increasing the flow rate Q induces a faster movement of the front, as A is injected with a higher speed into B . In contrast, higher values of γ correspond to the slower progression of the front, since more reactant A is needed to consume B at a given distance from the injection site. The width h of the gap does not have any impact on the front position. In this long-time regime, the region of maximum concentration of the product C is located at the front position, $r_{c,A} = r_{f,A}$, regardless of the value of γ

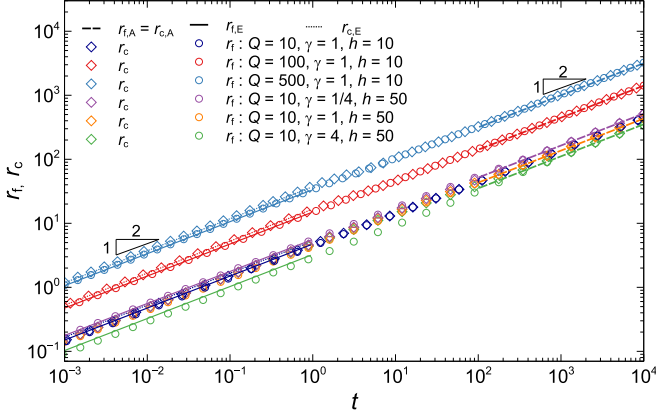


FIG. 6. Temporal evolution of r_f and r_c . Solid, dotted, and dashed lines represent Eq. (21a), Eq. (23), and Eq. (11), respectively.

(Fig. 6). This feature was also observed for RDA fronts in 1D polar [29] and 1D spherical [32] radial systems.

B. Production rate

Since in the long-time regime the concentrations of reactants and product are independent of z , the definitions (8) of the production rate are equivalent. Specifically, the maximum values of R and \tilde{R} in the Taylor dispersion regime are given by [29]

$$R_A^{\max}(t) = \tilde{R}_A^{\max}(t) \simeq \frac{29}{\pi^4} K^{4/3} t^{-2/3}, \quad (13)$$

where $K = (1 + \gamma)\Gamma^{-1}(Q/2)\mathcal{K}^{(Q-1)/2}e^{-\mathcal{K}}$. Figure 7 shows the temporal evolution of R^{\max} and \tilde{R}^{\max} obtained by solving Eqs. (3) numerically. Notice that for large flow rates, the maximum production rate is essentially independent of Q in the long-time regime and is fully governed by the reaction process through the dependence on γ . We observe that while \tilde{R}^{\max} directly switches from the early-time behavior to the long-time regime, R^{\max} exhibits an intermediate-regime behavior. In Appendix B we show that $R \geq \tilde{R}$ pointwise and therefore $R^{\max} \geq \tilde{R}^{\max}$, as is clearly seen in this intermediate regime.

C. Front width

The temporal evolution of w and \tilde{w} , shown in Fig. 8, exhibits a different behavior in the transient and short-time regimes, while their asymptotic long-time limits, w_A and \tilde{w}_A , converge to

$$w_A = \tilde{w}_A \simeq \pi K^{-1/3} t^{1/6}, \quad (14)$$

as for the 1D polar fronts case [29].

In Appendix C, we show that the width of the radial gradient of $\langle u \rangle = \langle a - b \rangle$ is given in the long-time limit by Eq. (C17). Because the width of the radial profile of $\langle c \rangle$ exhibits a similar behavior, we describe its temporal evolution by using the same functional as done in [33]. Hence, we find that the width w_c , shown in Fig. 9, of the average radial con-

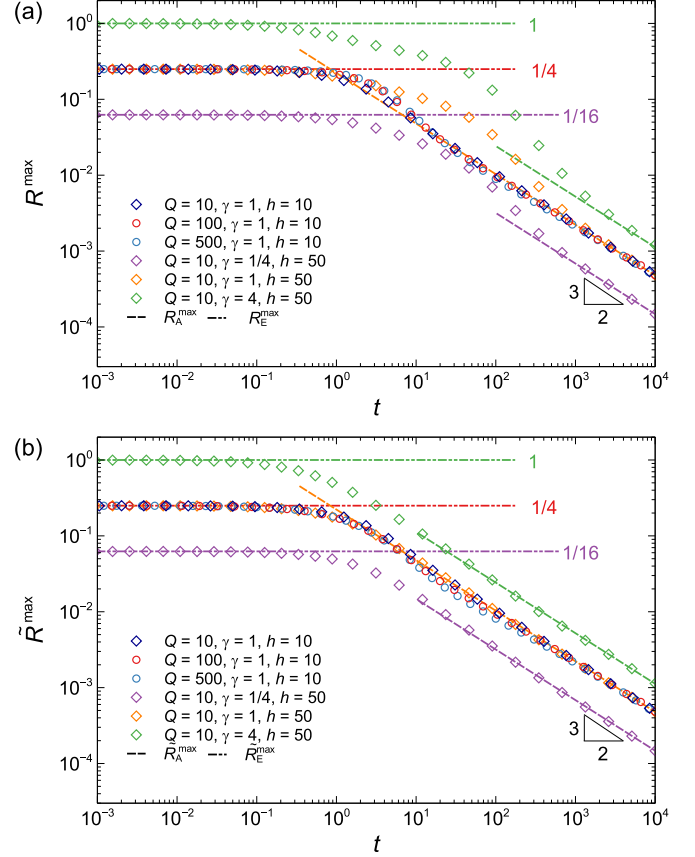


FIG. 7. Temporal evolution of (a) R^{\max} and (b) \tilde{R}^{\max} . The dashed lines represent Eq. (13), the dashed-dotted lines represent Eq. (25).

centration profile $\langle c \rangle$ is approximated in the long-time limit by

$$w_{c,TA}(t) \simeq c_\gamma \sqrt{\frac{4}{3}t + t_c}, \quad t_c = \frac{Qh^2}{115}, \quad (15a)$$

$$c_\gamma(\gamma) = \frac{1}{2} \left(\frac{1-\gamma}{1+\gamma} \right)^2 + 0.03 \left(\frac{1-\gamma}{1+\gamma} \right) + 1.23, \quad (15b)$$

where c_γ is obtained through numerical fitting, as shown in the inset of Fig. 9. The index TA stands for transient and asymptotic long-time regimes. Notice that the coefficient $4/3$ in Eq. (15a) accounts for the long-time limit of w_c in the 1D polar case, i.e., $w_{c,A}^{1D} = \sqrt{4t/3}$, as shown in Appendix D. In dimensional units, Eq. (15a) reads

$$\tilde{w}_{c,TA}(\bar{t}) = c_\gamma \sqrt{\frac{4}{3}D\bar{t} + D\bar{t}_c}, \quad \bar{t}_c = \frac{\bar{Q}\bar{h}}{230\pi D^2}. \quad (16)$$

For $\gamma = 1$, the latter expression is approximated as $\tilde{w}_{c,TA} \simeq \sqrt{2D\bar{t}(1 + 3\bar{t}_c/4\bar{t})}$. Notice that Eq. (15a) also describes w_c in the transient regime, for $t \lesssim t_c$, as we will discuss in Sec. VB.

D. Total amount of product

In the long-time regime, the calculation of the total amount of product given by Eq. (9) simplifies to $n_{c,A}(t) = 2\pi h \int rc(r,t)dr$ due the independence of z of the concentration of C . Hence, the following result from the 1D polar

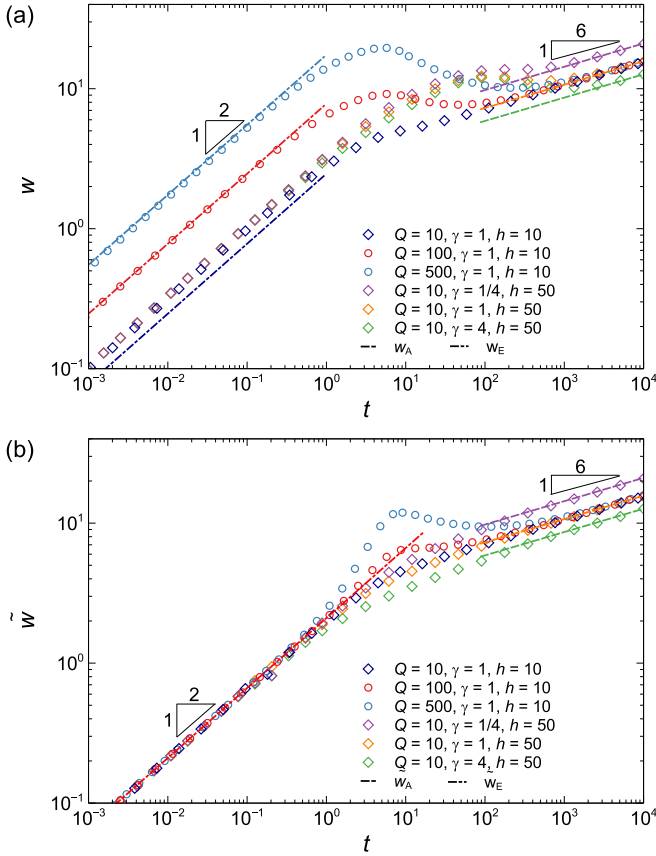


FIG. 8. Temporal evolution of (a) w and (b) \tilde{w} . The dashed lines represent Eq. (14), the dashed-dotted lines represent Eqs. (26) and (27).

system holds [29]:

$$n_{c,A}(t) \simeq \frac{116}{\pi^2} \alpha h K(Q, \gamma) \mathcal{K}^{1/2}(Q, \gamma) t. \quad (17)$$

The coefficient $\alpha \simeq 1.1$ is a constant whose value is obtained by fitting the numerical results shown in Fig. 10. Experimental

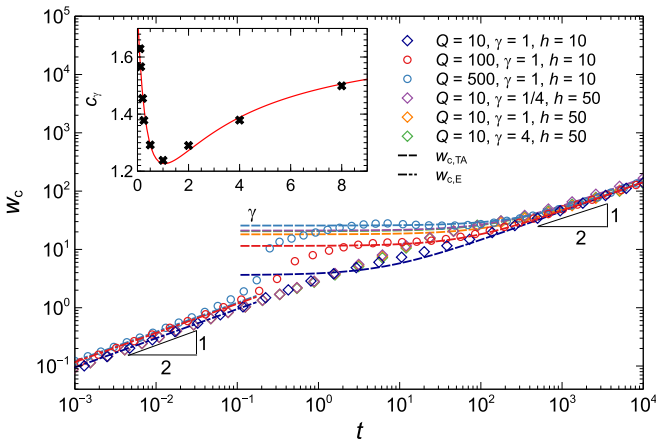


FIG. 9. Temporal evolution of w_c . The dashed lines represent Eq. (15a) and the dashed-dotted lines represent Eq. (28). Inset: Coefficient c_γ obtained from numerical computations with $Q = 100$ and $h = 20$. The solid line represents Eq. (15b).

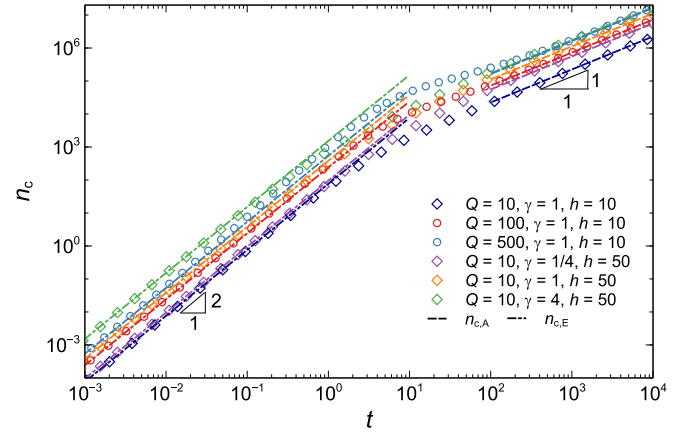


FIG. 10. Temporal evolution of the total amount of product. The dashed lines represent Eq. (17). The dashed-dotted lines represent Eq. (29).

data of Ref. [33] show that the dimensional total amount of product can be expressed in terms of the injected volume $\bar{V} = \bar{Q}\bar{t}$ of A through the linear relation

$$\bar{n}_{c,A}(\bar{V}) = \bar{a}_0 S_{th} \bar{V} + \bar{p}, \quad S_{th} = j(\gamma) Q^{-\beta(h)}, \quad (18)$$

where j , β , and \bar{p} are fitting parameters. In dimensionless units, Eq. (18) reads

$$n_{c,A}(V) = S_{th} V + p, \quad V = 2\pi h Q t, \quad (19)$$

where $\bar{n}_{c,A}$ and \bar{p} are both rescaled by $\bar{a}_0 \ell^3$. Experiments showed that $\beta \simeq 1/2$ for small gaps, and $\beta < 1/2$ for large values of h [33]. This is confirmed by our numerical computations, for which the dependence of the slope S_{th} on Q is shown in Fig. 11. For values of γ in the range [0.1–10], the coefficient $j(\gamma)$ can be approximated with (see the inset of Fig. 11)

$$j(\gamma) \simeq 0.57 \ln(1 + 4.5\gamma). \quad (20)$$

This expression is similar to what was found in [29], where the value $\beta = 1/2$ was used. The difference in the multiplicative coefficient that we observe here is traced back to the use of the

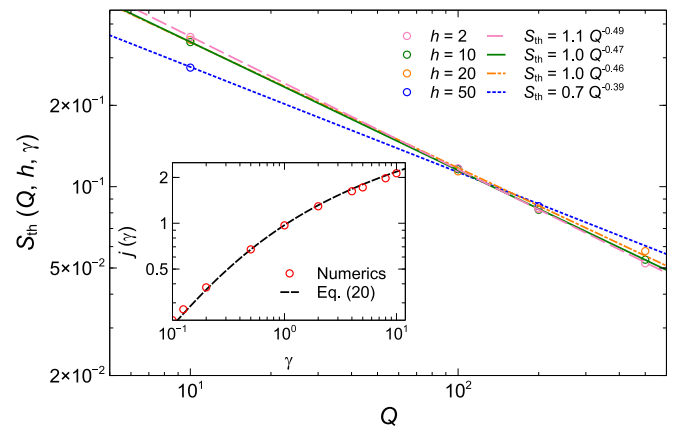


FIG. 11. Total amount of product as a function of the injected volume of A from numerical computations. The lines represent Eq. (19). Inset: Fit of S_{th} obtained from numerical analysis with $\gamma = 1$.

value of $\beta(h)$ obtained from the numerical fit of S_{th} and which is slightly different from $1/2$ (e.g., $\beta = 0.46$ for $h = 20$).

V. PREASYMPTOTIC DYNAMICS

The temporal evolution of the system at preasymptotic times is characterized by two distinct regimes, namely the early-time and the transient-time regimes. The analytical derivation of the results relative to the early-time regime is carried out in Appendix E.

A. The early-time regime

For 1D polar [29,31] and spherical [32] systems, the early-time regime is characterized by a small amount of diffusive mixing and thus solutions for the concentration fields a and b are obtained by neglecting the reaction term in the governing PDEs. The derivation of analytical early-time solutions is carried out in Appendix E by assuming that transverse diffusion can be neglected in this regime. This means that transport occurs along independent streamlines. In the following, we summarize the analytical results and the numerical computation analysis for the early-time regime.

1. Front position

We indicate the early-time limit of the front position as r_{fE} . In Appendix E, we show that it can be approximated as

$$r_{f,E}(t) \simeq 2\sqrt{K_E t}, \tag{21a}$$

$$K_E = \frac{0.9Q}{1 + 0.6\gamma}, \quad \text{for } Q \gg 1, \gamma \gtrsim 1, \tag{21b}$$

where the index E stands for early time. Notice that Eq. (21a) has the same form as for the long-time 1D polar system [29], except that the specific expression of K_E is different. When the reactants A and B are in equal initial concentration, i.e., when $\gamma = 1$, Eq. (21a) reduces to

$$r_{f,E}(\gamma = 1) \simeq \sqrt{2.25Qt}. \tag{22}$$

The radial position r_c where the average concentration of the product is maximum scales at early times as $r_c = r_{c,E} \propto Q^{1/2}t^{1/2}$. It is not surprising that this quantity exhibits the same dependence on the flow rate as $r_{f,E}$. However, numerical computations (see Fig. 6) show that $r_{c,E}$ does not depend significantly on γ , which means that it only depends on transport and not on reaction parameters. We obtain

$$r_{c,E}(t) = c_r(Q)t^{1/2} \simeq \frac{5}{3}Q^{1/2}t^{1/2}, \tag{23}$$

where $c_r(Q)$ is determined numerically and shown in Fig. 12. By comparing Eqs. (21a), (21b), and (23) we observe that $r_{c,E}$ is delayed with respect to $r_{f,E}$ when $\gamma \lesssim 1/2$, and advanced otherwise.

2. Production rate

Because in this early-time regime we neglect the reaction term in Eq. (3), the equations for a and b are identical. Hence, if a_E is a solution that satisfies the boundary conditions $a_E(0, z, t) = 1$ and $a_E(r \rightarrow \infty, z, t) = 0$, then $b_E = \gamma(1 - a_E)$ is also a solution that satisfies the boundary conditions $b_E(0, z, t) = 0$ and $b_E(r \rightarrow \infty, z, t) = \gamma$. Hence, the

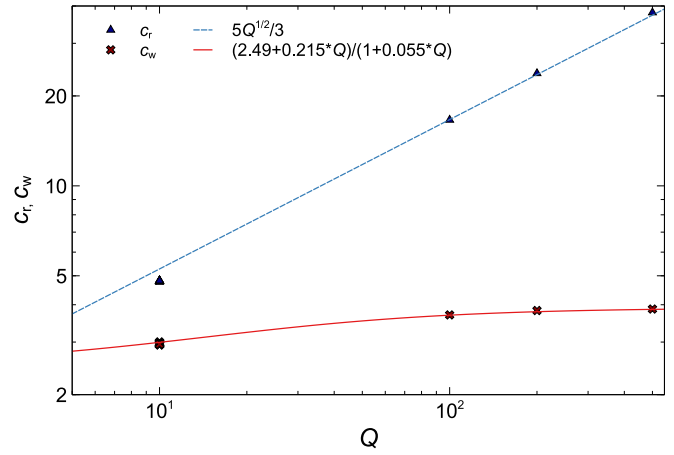


FIG. 12. Coefficients of c_r and c_w from numerical results obtained from different values of $Q \in [10, 500]$, $\gamma \in [0.1, 4]$, and $h \in [10, 200]$.

production rate at early times reduces to

$$R_E(r, z, t) = a_E(r, z, t)b_E(r, z, t) = \gamma a_E(r, z, t)[1 - a_E(r, z, t)]. \tag{24}$$

Its maximum along the radial direction is obtained by setting $\partial_r R_E|_{r=r_{max}} = 0$, where r_{max} is the radial coordinate of the maximum of R_E . This implies $a(r, z, t) = 1/2$ and thus $b(r, z, t) = \gamma/2$. Since these quantities do not depend on z , $R_E^{max} = \max(\langle a_E \rangle \langle b_E \rangle)$ and $\tilde{R}_E^{max} = \max(\langle a_E b_E \rangle)$ are equal and

$$R_E^{max} = \tilde{R}_E^{max} = \frac{\gamma}{4}. \tag{25}$$

Figure 7 shows the good agreement between Eq. (25) and the numerical solutions of Eq. (3) at short time. In this regime, the production rate is constant and it increases as γ is increased, which can be traced back to the larger availability of reactants. These results confirm that the maximum production rate at early times does not depend on the geometry of the system. Indeed, the same result was found for rectilinear reaction-diffusion fronts [45], as well as for 1D polar [29,31] and spherical [32] reaction-diffusion-advection fronts.

3. Reaction front width

The reaction front width at early times is defined here as the width at half height of the production rate. Because the definition of the latter is twofold, we define w_E as the width of $R_E = \langle a \rangle \langle b \rangle$ and \tilde{w}_E as the width of $\tilde{R}_E = \langle ab \rangle$. In this early-time regime, both quantities increase as $t^{1/2}$. Indeed, this scaling appears to be independent of the geometry, as it holds for rectilinear RD fronts [45], and 1D polar [29,31] and spherical [32] RDA fronts. However, the multiplicative coefficients depend on the geometry. In Appendix E, we derive that the width w_E of R_E grows at early times as

$$w_E \simeq 0.78 Q^{1/2} t^{1/2}, \tag{26}$$

as shown in Fig. 8(a). Notice that increasing the flow rate leads to a wider R_E profile. In contrast, numerical results show that \tilde{w}_E does not depend on the system parameters. This feature was also observed for the early-time front width in spherical

geometry [32]. The multiplicative constant depends on the geometry of the system. Here, by fitting on the numerical solution shown in Fig. 8(b), we find

$$\tilde{w}_E \simeq 2.1 t^{1/2}. \quad (27)$$

The width at half height of the average product $\langle c \rangle$ at early times also scales as $t^{1/2}$

$$w_{c,E} = c_w(Q) t^{1/2}, \quad c_w(Q) \simeq \frac{2.49 + 0.215Q}{1 + 0.055Q}, \quad (28)$$

where $c_w(Q)$ is a real coefficient determined numerically. The temporal evolution of $w_{c,E}$ at early times is shown in Fig. 9, while the coefficient c_w is shown in Fig. 12.

4. Total amount of product

The total amount of product n_c exhibits a ballistic growth in the early-time regime, $n_{c,E} \propto \gamma h Q^{1/2} t^2$. This scaling is characteristic of 1D polar injection in the early-time regime [29]. The effect of the nonhomogeneous flow field along z on the total amount of product appears only in the multiplicative constant. As shown in Appendix E, we have

$$n_{c,E}(t) \simeq \frac{\sqrt{3\pi^3}}{4} \gamma h Q^{1/2} t^2. \quad (29)$$

Numerical results are shown in Fig. 10, where good agreement with Eq. (29) is observed.

B. The transient-time regime

In the transient-time regime, the Poiseuille flow field bends the concentration profiles along z . This regime lasts until diffusion along z has homogenized the concentrations across the gap, thus until the occurrence of Taylor dispersion. The presence of a curvature in the z -direction concentration profiles has two fundamental consequences. First, it makes the 1D polar theories developed in [29,31], which assume the symmetry along the z axis, not applicable for this regime. Second, it has a different impact on average quantities, according to how the average is computed. In fact, the production rates $R = \langle a \rangle \langle b \rangle$ and $\tilde{R} = \langle ab \rangle$ exhibit significant differences in the transient regime, as explained in Sec. IV, which is reflected in the maximum production rates R^{\max} and \tilde{R}^{\max} , as well as in the front widths w and \tilde{w} , as shown in Fig. 13.

Specifically, tilded quantities diverge from the 1D polar behavior less than the corresponding nontilded quantities. It is not surprising that the deviation from the 1D polar case is larger for larger values of the gap aperture h . Because front dynamics in the transient regime is strongly nonlinear, analytical expressions are not trivial to find. Nevertheless, Eq. (15a) describes the evolution of w_c in the transient and the long-time regimes. The time t_c represents a transition timescale, as we shall discuss in Sec. V C. For $t \lesssim t_c$, a plateau is observed which indicates that the width of C does not vary in time. In fact, in this regime the front progresses radially but does not spread around its mean position. This is due to the contrasting effect of diffusion, which enhances spreading, and reaction that consumes the outermost part of reactant A. Equation (15a) reproduces with good agreement the numerical results, as shown in Fig. 9. Notice that in order for the transient regime to be observed, a condition on the transition timescales must be

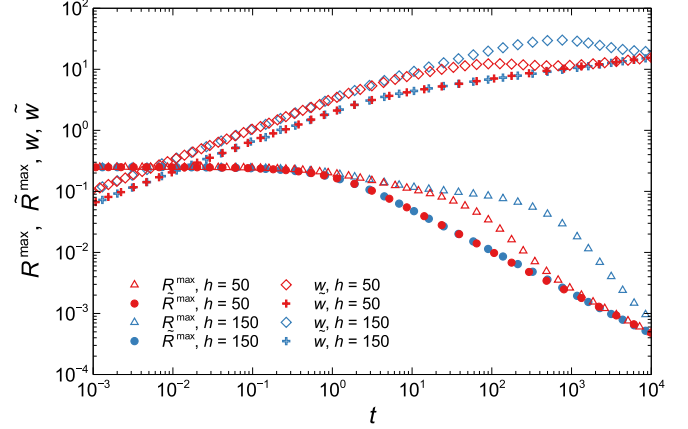


FIG. 13. Temporal evolution of R^{\max} , \tilde{R}^{\max} , w , and \tilde{w} for $Q = 10$ and $\gamma = 1$.

fulfilled. Specifically, we must require that t_c be much larger than the transition timescale t_{ET} between the early- and the transient-time regimes.

C. Transition timescales

The transition time t_{ET} between the early and the transient regime can be estimated by using the early-time and the asymptotic long-time expressions of \tilde{R}^{\max} , in analogy to what was done for spherical fronts [32]. Indeed, as we showed in the previous section, \tilde{R}^{\max} behaves in the same way in the transient- and in the long-time regimes. Thus, by equating the right-hand side terms of Eqs. (25) and (13), we get

$$t_{ET} = \frac{232\sqrt{29}K^2}{(\gamma\pi^4)^{3/2}} \stackrel{Q \gg 1}{\simeq} \frac{464\sqrt{29}}{\pi^6\gamma^{3/2}} \ln(1 + \gamma/\sqrt{2\pi}), \quad (30)$$

where the approximation $K \stackrel{Q \gg 1}{\simeq} \sqrt{2 \ln(1 + \gamma/\sqrt{2\pi})}$ was used [29].

We can define the transition time between the transient- and the long-time regimes in two ways. According to the first definition, the transition time is the time t_{Ta} at which the Taylor regime arises. It is found by requiring that $E(r) \ll 1$ in Eq. (10). In Appendix A, we show that

$$t_{Ta} = \frac{Q^2 h^2}{840K(Q, \gamma)}. \quad (31)$$

According to this definition, the condition to observe the transient-time regime $t_{Ta} \gg t_{ET}$ reads

$$h \gg h_c(Q, \gamma) \simeq \frac{2^{10} \mathcal{K}^{1/2}(Q, \gamma) K(Q, \gamma)}{\gamma^{3/4} \pi^3 Q}. \quad (32)$$

For $Q \gg 1$, we can use the approximation [29] $\mathcal{K}^{1/2}(Q, \gamma) K(Q, \gamma) \simeq j(\gamma) Q^{1/2}$, where $j(\gamma)$ is given by Eq. (20), while for $Q \rightarrow 0$, $\mathcal{K}^{1/2}(Q, \gamma) K(Q, \gamma)/Q \rightarrow 1/2$. Thus, we obtain

$$h_c(Q, \gamma) \simeq \begin{cases} \frac{2^{10} j(\gamma)}{\gamma^{3/4} \pi^3 Q^{1/2}}, & Q \gg 1, \\ \frac{2^9}{\gamma^{3/4} \pi^3}, & Q \ll 1. \end{cases} \quad (33)$$

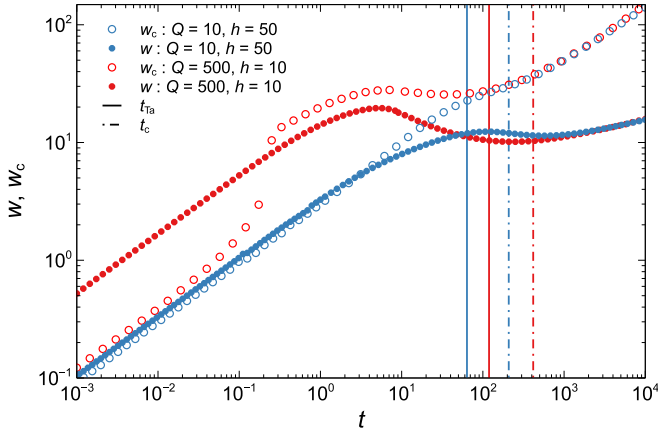


FIG. 14. Temporal evolution of w and w_c . The solid lines are the transition time (31) and the dashed lines indicate the transition time (15a).

Notice that for small flow rates, the value of the critical gap width h_c beyond which the transient-time regime is observed does not depend on Q . For example, by using Eq. (32), we find $h_c = 5.7$ for $\gamma = 1$ and $Q = 10$, which explains why the transient regime is not visible in Fig. 9 for $h = 10$, which is not large enough compared to h_c . In contrast, it is visible for $Q = 500$, $\gamma = 1$, $h = 10$ since $h_c = 0.8$.

The second definition of the transition time between the transient- and the long-time regimes is based on the temporal evolution of the product width w_c . We indicate this time scale by t_c as defined in Eq. (15a). These timescales are shown in Fig. 14 for two distinct sets of parameters. Notice that because $\mathcal{K}(Q, g) \simeq Q/2$ when $Q \gg 1$ [29], t_c and t_{Ta} differ only by a constant factor at large flow rates. For experimental purposes, however, the choice of t_c , Eq. (15a), as the transition time is preferable, as it directly refers to the width w_c of the product, a quantity that can be measured in laboratory experiments.

To provide an example of the timescales at which the different time regimes arise in real laboratory conditions, we refer to the recent experiment presented in Ref. [33], where for $\bar{a}_0 = 0.03$ M and $k = 200$ M $^{-1}$ s $^{-1}$ the characteristic time of the reaction is $\tau = 0.167$ s. The diffusion coefficient in the experiment is $D = 4 \times 10^{-10}$ m 2 /s. The smallest flow rate used is $\bar{Q} = 0.01$ mL/min, which, in virtue of Eq. (4), implies $Q \simeq 368$, so that the approximations for $Q \gg 1$ hold. Hence, by using Eq. (30), the dimensional transition timescale \bar{t}_{ET} between the early- and the transient-time regimes is $\bar{t}_{ET} = \tau t_{ET} \simeq 0.15$ s. Notice that this time increases if the reactant A is in a smaller initial concentration and/or if the reaction is slower, i.e., for smaller values of the kinetic constant k .

By using Eq. (16), we estimate the dimensional transition time \bar{t}_c between the transient- and the long-time asymptotic regimes. We use the narrowest gap used in Ref. [33], namely $\bar{h} = 0.18$ mm, and $\bar{Q} = 0.01$ mL/min, and we obtain $\bar{t}_c \simeq 260$ s. This timescale is larger for larger values of the flow rate and for higher gaps.

VI. CONCLUSIONS

We have studied the effect of a nonuniform advection field on the dynamics of $A + B \rightarrow C$ fronts when A is injected

radially into B . To this end, we have considered the Poiseuille flow as it describes the velocity field in a volume confined by two parallel plates, such as in a Hele-Shaw cell. The interplay between transport and reaction processes gives rise to a complex front dynamics, which we have characterized from the numerical and theoretical viewpoints. To derive predictions that can provide relevant insight to experimental works, we have studied the behavior of the observables averaged over the gap separating the boundaries. Specifically, we have performed the analysis of the front position, the maximum and the width of the production rate, the position and the width of the radial concentration profile of the product, as well as its total amount. This analysis reveals the occurrence of three distinct temporal regimes.

The early-time regime is characterized by a small amount of mixing of the reactants. Therefore, the impact of reaction is also small. In this regime, the vertically averaged front position $r_{f,E}$ and the position $r_{c,E}$ of maximum product concentration both scale as $t^{1/2}$, as expressed in Eqs. (21a) and (23), respectively. The same temporal scaling is observed for the front width w_E and \tilde{w}_E , as well as the width w_c of the product profile, see Eqs. (26)–(28), while the total amount of product $n_{c,E} \sim t^2$ (29). While these are common features of 1D radial fronts, the multiplicative coefficients of the various scalings depend on the specific geometry, hence on the velocity profile. In contrast, the maximum of the production rate $R_E^{\max} = \tilde{R}_E^{\max} = \gamma/4$ is independent of the geometry.

The transient regime is characterized by the interplay of diffusion, advection, and reaction. In this regime, the concentration profiles of the reactants are bent and stretched by the Poiseuille flow. On the other hand, diffusion tends to smooth the gradients of concentration. These contrasting mechanisms enhance the formation of the plateau that is observed in the temporal evolution of w_c , Eq. (15a). In this and the following regime, reaction is important and it opposes itself to the front expansion due to passive advection. Because of these processes, the front dynamics in the transient regime is complex and it has been described from a numerical point of view.

Finally, in the long-time regime, we retrieve the same dynamics as in the purely 1D radial system. This is explained in terms of Taylor dispersion, generalized here to the considered radial reactive system. This means that in the long-time limit, transverse diffusion homogenizes the system in the z direction and the problem becomes effectively one-dimensional. As a consequence, all the analytical results for the 1D polar system [29] apply here in this asymptotic limit. As for the other radial front systems, and in contrast to rectilinear injection, the flow rate Q can here be tuned to control the front dynamics as well as the total amount of product.

The results presented in this work shed light on the impact of nonuniform velocity fields on 2D radial reaction fronts and can be used as predictive tools to analyze experimental data.

ACKNOWLEDGMENTS

This project has received funding from the European Union's Horizon 2020 research and innovation programme under the Marie Skłodowska-Curie Grant Agreement No.

801505, and from the PRODEX Grant CHYPI. A.D. acknowledges funding from FRS-FNRS through the PDR grant CONTROL.

APPENDIX A: TAYLOR DISPERSION

The system is characterized by four distinct timescales, namely

- (i) the chemical timescale: $\tau = 1/k\bar{a}_0$;
- (ii) the diffusion time along z : $\bar{t}_D = \bar{h}^2/D$;
- (iii) the advection time: $\bar{T}_A = \bar{\rho}/\bar{v}_m(\bar{\rho})$;
- (iv) the diffusion time along r : $\bar{T}_D = \bar{\rho}^2/D$;

where \bar{v}_m is given by Eq. (2) and $\bar{\rho}$ is a characteristic length scale of advection that is typically much larger than the aperture gap \bar{h} and

$$\bar{v}_m(\bar{\rho}) = \frac{3\bar{Q}}{4\pi\bar{h}\bar{\rho}}, \quad \epsilon = \frac{\bar{h}}{\bar{\rho}} \ll 1. \quad (\text{A1})$$

Hence, $\bar{T}_D \gg \bar{t}_D$. Moreover, in the radial direction advection occurs on a shorter timescale than diffusion, i.e., $\bar{T}_A \ll \bar{T}_D$, when

$$\bar{Q} \gg \frac{4}{3}\pi\bar{h}D. \quad (\text{A2})$$

Condition (A2) establishes the smallest flow rate that is needed to observe Taylor dispersion. For $\bar{h} = 0.5$ mm and $D = 10^{-9}$ m²/s, the minimum flow rate is $\bar{Q} \simeq 10^{-12}$ m³/s = 1 nl/s. We consider here systems for which $\bar{t}_D \ll \tau \sim \bar{T}_A \ll \bar{T}_D$, which is satisfied when \bar{h} or k are small and Q is large enough [see Eq. (A2)]. The long-time dynamics is characterized by two distinct timescales, namely the advection time \bar{T}_A and the dispersion time \bar{T}_D .

The dimensional equation for the conservative component $\bar{u} = \bar{a} - \bar{b}$ is obtained by subtracting Eq. (1b) from Eq. (1a),

$$\partial_{\bar{t}}\bar{u} + (\bar{\mathbf{v}} \cdot \bar{\nabla})\bar{u} = D\bar{\nabla}^2\bar{u}. \quad (\text{A3})$$

The initial and boundary conditions for u are derived from those of the reactant concentrations and read $u(r, z, 0) = 1 - (1 + \gamma)H(r)$, $u(r = 0, z, t) = 1$, $u(r \rightarrow \infty, z, t) = -\gamma$, and $\partial_z u(r, z = \pm h/2, t) = 0$, where $H(\cdot)$ is the Heaviside function. In order to derive equations for the z -averaged concentrations in the long-time regime, we perform a multiple-scale analysis for $\bar{t} \gtrsim \bar{T}_A$. First, we nondimensionalize the equations by rescaling the lengths and times as

$$\tilde{r} = \bar{r}/\bar{\rho}, \quad \tilde{z} = \bar{z}/\bar{h}, \quad \tilde{t} = \bar{t}/\bar{T}_A, \quad \tilde{\tau} = \tau/\bar{T}_A, \quad (\text{A4})$$

and the velocity, given in Eq. (2), as

$$\tilde{v}_r(\tilde{r}, \tilde{z}) = \frac{\bar{v}_r(\bar{\rho}\tilde{r}, \bar{\rho}\tilde{z})}{\bar{v}_m(\bar{\rho})} = \frac{\bar{v}_m(\bar{\rho}\tilde{r})}{\bar{v}_m(\bar{\rho})}\tilde{v}_r^{(z)}(\tilde{z}) = \frac{\tilde{v}_r^{(z)}(\tilde{z})}{\tilde{r}}, \quad (\text{A5a})$$

$$\text{with } \tilde{v}_r^{(z)}(\tilde{z}) = 1 - 4\tilde{z}^2, \quad (\text{A5b})$$

and where tilde denotes nondimensional quantities. Concentrations are rescaled by the initial concentration of A as in the main text. Hence, by substituting these expressions into Eqs. (1a) and (A3) we get for a and u

$$\begin{aligned} \text{Pe}(\bar{\rho})\epsilon \left[\frac{\partial a}{\partial \tilde{t}} + \frac{\tilde{v}_r^{(z)}}{\tilde{r}} \frac{\partial a}{\partial \tilde{r}} \right] \\ = \epsilon^2 \left[\frac{\partial^2 a}{\partial \tilde{r}^2} + \frac{1}{\tilde{r}} \frac{\partial a}{\partial \tilde{r}} \right] + \frac{\partial^2 a}{\partial \tilde{z}^2} - \frac{\text{Pe}(\bar{\rho})}{\tilde{\tau}} \epsilon a(a - u) \end{aligned} \quad (\text{A6})$$

and

$$\text{Pe}(\bar{\rho})\epsilon \left[\frac{\partial u}{\partial \tilde{t}} + \frac{\tilde{v}_r^{(z)}}{\tilde{r}} \frac{\partial u}{\partial \tilde{r}} \right] = \epsilon^2 \left[\frac{\partial^2 u}{\partial \tilde{r}^2} + \frac{1}{\tilde{r}} \frac{\partial u}{\partial \tilde{r}} \right] + \frac{\partial^2 u}{\partial \tilde{z}^2}, \quad (\text{A7})$$

where $\text{Pe}(\bar{\rho}) = \bar{v}_m(\bar{\rho})\bar{h}/D$ is the Péclet number. We assume that all terms are of order 1, except for $\epsilon \ll 1$. Hence, $\text{Pe}(\bar{\rho})$ is assumed of order 1 and by using Eq. (A1) we obtain

$$\bar{\rho} \sim 3\bar{Q}/(4\pi D). \quad (\text{A8})$$

Moreover, since $\text{Pe}(\bar{\rho})$ is of order 1, we must have $\tilde{\tau}$ of order 1 in Eq. (A6). Thus, $\tau \sim \bar{T}_A$ which implies

$$\bar{\rho} \sim \sqrt{\frac{3\bar{Q}\tau}{4\pi\bar{h}}}. \quad (\text{A9})$$

Since both Pe and $\tilde{\tau}$ are of order 1, we have $\tilde{\tau} \sim \text{Pe}$. This is equivalent to $\tau \sim t_D/\epsilon$ which is consistent with the assumption $\tau \gg t_D$ made above since $\epsilon \ll 1$. If this condition is verified, then the term $\text{Pe}/\tilde{\tau}$ in Eq. (A6) is of order 1 and ϵ is the only small parameter. By combining Eqs. (A8) and (A9) we obtain $\bar{h} \sim 4\pi D^2/(3\bar{Q}k\bar{a}_0)$, which implies small values of k and/or \bar{Q} and/or \bar{a}_0 to have a value of \bar{h} comparable to the one used usually in experiments. In dimensionless units, the condition reduces to $h \sim Q^{-1/2}$. Although these requirements are quite restrictive, we find that the approximated equations (10) that we derive in the following hold on a much broader domain of validity, as we showed in the main text.

We assume that the solutions depend on two different timescales. A short timescale, $t_0 = \tilde{t}$, and a long timescale, $t_1 = \epsilon\tilde{t}$, so that t_1 is of order 1 when t_0 is of order $\epsilon^{-1} \gg 1$. Therefore, the time derivative becomes

$$\partial_{\tilde{t}} = \partial_{t_0} + \epsilon \partial_{t_1}. \quad (\text{A10})$$

In addition, we introduce the following expansion,

$$x = x_0 + \epsilon x_1 + \epsilon^2 x_2 + O(\epsilon^3), \quad (\text{A11})$$

where x stands for a or u . By substituting the expansions (A10) and (A11) into Eqs. (A6) and (A7) and solving order by order up to the second order in ϵ , we obtain the following expressions.

Order ϵ^0 :

$$\partial_{\tilde{z}}^2 a^{(0)} = 0 \quad \Rightarrow \quad a^{(0)} = a^{(0)}(\tilde{r}, t_0, t_1), \quad (\text{A12a})$$

$$\partial_{\tilde{z}}^2 u^{(0)} = 0 \quad \Rightarrow \quad u^{(0)} = u^{(0)}(\tilde{r}, t_0, t_1). \quad (\text{A12b})$$

These equations imply that both $a^{(0)}$ and $u^{(0)}$ do not depend on \tilde{z} because of the zero-flux boundary conditions at the reactor walls $\partial_{\tilde{z}} a^{(0)}|_{\tilde{z}=\pm 1/2} = \partial_{\tilde{z}} u^{(0)}|_{\tilde{z}=\pm 1/2} = 0$.

Order ϵ^1 :

$$\begin{aligned} \text{Pe}(\bar{\rho}) \left[\partial_{t_0} a^{(0)} + \frac{\tilde{v}_r^{(z)}}{\tilde{r}} \partial_{\tilde{r}} a^{(0)} \right] \\ = \partial_{\tilde{z}}^2 a^{(1)} - \frac{\text{Pe}(\bar{\rho})}{\tilde{\tau}} a^{(0)} [a^{(0)} - u^{(0)}], \end{aligned} \quad (\text{A13a})$$

$$\text{Pe}(\bar{\rho}) \left[\partial_{t_0} u^{(0)} + \frac{\tilde{v}_r^{(z)}}{\tilde{r}} \partial_{\tilde{r}} u^{(0)} \right] = \partial_{\tilde{z}}^2 u^{(1)}. \quad (\text{A13b})$$

By averaging Eq. (A13) over \tilde{z} using Eq. (5), the second-order z -derivative terms cancel out because of the zero-flux

boundary conditions at $\tilde{z} = \pm 1/2$. Thus, we obtain

$$\text{Pe}(\bar{\rho}) \left[\partial_{\tilde{t}_0} a^{(0)} + \frac{\langle \tilde{v}_r^{(z)} \rangle}{\tilde{r}} \partial_{\tilde{r}} a^{(0)} + \frac{a^{(0)}(a^{(0)} - u^{(0)})}{\tilde{\tau}} \right] = 0, \quad (\text{A14a})$$

$$\text{Pe}(\bar{\rho}) \left[\partial_{\tilde{t}_0} u^{(0)} + \frac{\langle \tilde{v}_r^{(z)} \rangle}{\tilde{r}} \partial_{\tilde{r}} u^{(0)} \right] = 0. \quad (\text{A14b})$$

By subtracting these equations from Eq. (A13), we get

$$\frac{\text{Pe}(\bar{\rho})}{\tilde{r}} v(\tilde{z}) \partial_{\tilde{r}} a^{(0)} = \partial_{\tilde{z}}^2 a^{(1)}, \quad (\text{A15a})$$

$$\frac{\text{Pe}(\bar{\rho})}{\tilde{r}} v(\tilde{z}) \partial_{\tilde{r}} u^{(0)} = \partial_{\tilde{z}}^2 u^{(1)}, \quad (\text{A15b})$$

where $v(\tilde{z}) = \tilde{v}_r^{(z)} - \langle \tilde{v}_r^{(z)} \rangle = \tilde{v}_r^{(z)} - 2/3$ is a measure of the nonuniformity of the advective field across the gap. By substituting Eq. (A5b) into the latter, we obtain

$$v(\tilde{z}) = \frac{1}{3} - 4\tilde{z}^2. \quad (\text{A16})$$

Equations (A15) are solved by using the separation of variables method; i.e., let

$$a^{(1)}(\tilde{r}, \tilde{z}, \tilde{t}_0, \tilde{t}_1) = \frac{\text{Pe}(\bar{\rho})}{\tilde{r}} \partial_{\tilde{r}} a^{(0)} H(\tilde{z}), \quad (\text{A17a})$$

$$u^{(1)}(\tilde{r}, \tilde{z}, \tilde{t}_0, \tilde{t}_1) = \frac{\text{Pe}(\bar{\rho})}{\tilde{r}} \partial_{\tilde{r}} u^{(0)} H(\tilde{z}). \quad (\text{A17b})$$

Substituting these expressions into Eq. (A15) implies in both cases

$$d_{\tilde{z}}^2 H(\tilde{z}) = v(\tilde{z}), \quad (\text{A18})$$

with $d_{\tilde{z}} H(\tilde{z}) = 0$ at $\tilde{z} = \pm 1/2$. Solving Eq. (A18) gives $H(\tilde{z}) = \tilde{z}^2/6 - \tilde{z}^4/3 + c_H$. To compute the value of the integration constant c_H , we impose $\langle H \rangle = 0$, so that $\langle a^{(1)} \rangle = \langle u^{(1)} \rangle = 0$ and we obtain $c_H = -7/720$, which implies

$$H(\tilde{z}) = \frac{\tilde{z}^2}{6} - \frac{\tilde{z}^4}{3} - \frac{7}{720}. \quad (\text{A19})$$

Order ϵ^2 :

$$\text{Pe}(\bar{\rho}) \left[\partial_{\tilde{t}_0} a^{(1)} + \partial_{\tilde{t}_1} a^{(0)} + \frac{\tilde{v}_r^{(z)}}{\tilde{r}} \partial_{\tilde{r}} a^{(1)} \right] = \partial_{\tilde{r}}^2 a^{(0)} + \frac{\partial_{\tilde{r}} a^{(0)}}{\tilde{r}} + \partial_{\tilde{z}}^2 a^{(2)} + \frac{\text{Pe}(\bar{\rho})}{\tilde{\tau}} [-2a^{(0)}a^{(1)} + a^{(0)}u^{(1)} + a^{(1)}u^{(0)}], \quad (\text{A20a})$$

$$\text{Pe}(\bar{\rho}) \left[\partial_{\tilde{t}_0} u^{(1)} + \partial_{\tilde{t}_1} u^{(0)} + \frac{\tilde{v}_r^{(z)}}{\tilde{r}} \partial_{\tilde{r}} u^{(1)} \right] = \partial_{\tilde{r}}^2 u^{(0)} + \frac{\partial_{\tilde{r}} u^{(0)}}{\tilde{r}} + \partial_{\tilde{z}}^2 u^{(2)}. \quad (\text{A20b})$$

Substituting the expressions (A17) into (A20), we obtain

$$\begin{aligned} & \text{Pe}(\bar{\rho}) \left[\frac{\text{Pe}(\bar{\rho})H(\tilde{z})}{\tilde{r}} \left(\frac{\partial^2 a^{(0)}}{\partial_{\tilde{r}} \partial_{\tilde{t}_0}} - \frac{\tilde{v}_r^{(z)} \partial_{\tilde{r}} a^{(0)}}{\tilde{r}^2} + \frac{\tilde{v}_r^{(z)} \partial_{\tilde{r}}^2 a^{(0)}}{\tilde{r}} \right) + \partial_{\tilde{t}_1} a^{(0)} \right] \\ & = \partial_{\tilde{r}}^2 a^{(0)} + \frac{\partial_{\tilde{r}} a^{(0)}}{\tilde{r}} + \partial_{\tilde{z}}^2 a^{(2)} + \frac{\text{Pe}^2(\bar{\rho})H(\tilde{z})}{\tilde{\tau}\tilde{r}} [(u^{(0)} - 2a^{(0)})\partial_{\tilde{r}} a^{(0)} + a^{(0)}\partial_{\tilde{r}} u^{(0)}], \end{aligned} \quad (\text{A21a})$$

$$\text{Pe}(\bar{\rho}) \left[\frac{\text{Pe}(\bar{\rho})H(\tilde{z})}{\tilde{r}} \left(\frac{\partial^2 u^{(0)}}{\partial_{\tilde{r}} \partial_{\tilde{t}_0}} - \frac{\tilde{v}_r^{(z)} \partial_{\tilde{r}} u^{(0)}}{\tilde{r}^2} + \frac{\tilde{v}_r^{(z)} \partial_{\tilde{r}}^2 u^{(0)}}{\tilde{r}} \right) + \partial_{\tilde{t}_1} u^{(0)} \right] = \partial_{\tilde{r}}^2 u^{(0)} + \frac{\partial_{\tilde{r}} u^{(0)}}{\tilde{r}} + \partial_{\tilde{z}}^2 u^{(2)}. \quad (\text{A21b})$$

Notice that Eq. (A14) provides expressions for $\partial_{\tilde{t}_0} a^{(0)}$ and $\partial_{\tilde{t}_0} u^{(0)}$ which we substitute into Eq. (A21) to get

$$\frac{\text{Pe}^2(\bar{\rho})H(\tilde{z})v(\tilde{z})}{\tilde{r}^2} \left(\partial_{\tilde{r}}^2 a^{(0)} - \frac{\partial_{\tilde{r}} a^{(0)}}{\tilde{r}} \right) + \text{Pe}(\bar{\rho})\partial_{\tilde{t}_1} a^{(0)} = \partial_{\tilde{r}}^2 a^{(0)} + \frac{\partial_{\tilde{r}} a^{(0)}}{\tilde{r}} + \partial_{\tilde{z}}^2 a^{(2)}, \quad (\text{A22a})$$

$$\frac{\text{Pe}^2(\bar{\rho})H(\tilde{z})v(\tilde{z})}{\tilde{r}^2} \left(\partial_{\tilde{r}}^2 u^{(0)} - \frac{\partial_{\tilde{r}} u^{(0)}}{\tilde{r}} \right) + \text{Pe}(\bar{\rho})\partial_{\tilde{t}_1} u^{(0)} = \partial_{\tilde{r}}^2 u^{(0)} + \frac{\partial_{\tilde{r}} u^{(0)}}{\tilde{r}} + \partial_{\tilde{z}}^2 u^{(2)}. \quad (\text{A22b})$$

We perform the average over \tilde{z} of these equations by recalling that $a^{(0)}$ and $u^{(0)}$ do not depend on \tilde{z} . Hence

$$\text{Pe}(\bar{\rho})\partial_{\tilde{r}_1}a^{(0)} + \frac{\text{Pe}^2(\bar{\rho})\langle H(\tilde{z})v(\tilde{z}) \rangle}{\bar{r}^2} \left(\partial_{\tilde{r}}^2 a^{(0)} - \frac{\partial_{\tilde{r}} a^{(0)}}{\bar{r}} \right) = \partial_{\tilde{r}}^2 a^{(0)} + \frac{\partial_{\tilde{r}} a^{(0)}}{\bar{r}}, \quad (\text{A23a})$$

$$\text{Pe}(\bar{\rho})\partial_{\tilde{r}_1}u^{(0)} + \frac{\text{Pe}^2(\bar{\rho})\langle H(\tilde{z})v(\tilde{z}) \rangle}{\bar{r}^2} \left(\partial_{\tilde{r}}^2 u^{(0)} - \frac{\partial_{\tilde{r}} u^{(0)}}{\bar{r}} \right) = \partial_{\tilde{r}}^2 u^{(0)} + \frac{\partial_{\tilde{r}} u^{(0)}}{\bar{r}}, \quad (\text{A23b})$$

where we used again the zero-flux boundary conditions at $\tilde{z} = \pm 1/2$. Finally, we multiply Eqs. (A23) by ϵ and we sum them to Eq. (A14), and we obtain

$$\text{Pe}(\bar{\rho}) \left[\partial_{\tilde{r}} a^{(0)} + \frac{\langle \tilde{v}_r^{(z)} \rangle}{\bar{r}} \partial_{\tilde{r}} a^{(0)} + \frac{1}{\bar{r}} (a^{(0)2} - a^{(0)}u^{(0)}) \right] = \epsilon \left[E_+(\bar{r}) \partial_{\tilde{r}}^2 a^{(0)} + \frac{E_-(\bar{r})}{\bar{r}} \partial_{\tilde{r}} a^{(0)} \right], \quad (\text{A24a})$$

$$\text{Pe}(\bar{\rho}) \left[\partial_{\tilde{r}} u^{(0)} + \frac{\langle \tilde{v}_r^{(z)} \rangle}{\bar{r}} \partial_{\tilde{r}} u^{(0)} \right] = \epsilon \left[E_+(\bar{r}) \partial_{\tilde{r}}^2 u^{(0)} + \frac{E_-(\bar{r})}{\bar{r}} \partial_{\tilde{r}} u^{(0)} \right], \quad (\text{A24b})$$

where $\partial_{\tilde{r}} = \partial_{\tilde{r}_0} + \epsilon \partial_{\tilde{r}_1}$ and

$$E_{\pm}(\bar{r}) = 1 \mp \text{Pe}^2(\bar{\rho}) \langle H(\tilde{z})v(\tilde{z}) \rangle / \bar{r}^2. \quad (\text{A25})$$

The term $\langle Hv \rangle$ is computed by using Eq. (A19) and Eq. (A16) to obtain

$$\langle H(\tilde{z})v(\tilde{z}) \rangle = \int_{-1/2}^{1/2} \left(\frac{1}{3} - 4\tilde{z}^2 \right) \left(\frac{\tilde{z}^2}{6} - \frac{\tilde{z}^4}{3} - \frac{7}{720} \right) d\tilde{z} = -\frac{2}{945}. \quad (\text{A26})$$

Thus, Eq. (A25) reduces to

$$E_{\pm} = 1 \pm \frac{2 \text{Pe}^2(\bar{\rho})}{945 \bar{r}^2} = 1 \pm \frac{2 \text{Pe}^2(\bar{\rho}) \bar{\rho}^2}{945 \bar{r}^2}. \quad (\text{A27})$$

Notice that the average velocity across the gap is $\bar{V}_r(\bar{r}) = \langle \tilde{v}_r(\bar{r}, \tilde{z}) \rangle = 2\bar{v}_m(\bar{r})/3$. Therefore, by using the definition of the Péclet number, we have $\text{Pe}(\bar{\rho})\bar{\rho}/\bar{r} = \bar{v}_m(\bar{r})\bar{h}/D = 3\bar{V}_r\bar{h}/2D$. Using this relation in Eq. (A27), we obtain

$$E_{\pm} = 1 \pm \frac{\bar{V}_r^2(\bar{r})\bar{h}^2}{210 D^2}. \quad (\text{A28})$$

By converting Eqs. (A24) to dimensional units, and recalling that $\bar{a}^{(0)} - \bar{u}^{(0)} = \bar{b}^{(0)}$, we find

$$\partial_{\tilde{r}} \bar{a}^{(0)} + \bar{V}_r(r) \partial_{\tilde{r}} \bar{a}^{(0)} - D \left[\partial_{\tilde{r}}^2 \bar{a}^{(0)} + \frac{1}{\bar{r}} \partial_{\tilde{r}} \bar{a}^{(0)} \right] + k \bar{a}^{(0)} \bar{b}^{(0)} = D \bar{E} \left[\partial_{\tilde{r}}^2 \bar{a}^{(0)} - \frac{1}{\bar{r}} \partial_{\tilde{r}} \bar{a}^{(0)} \right], \quad (\text{A29a})$$

$$\partial_{\tilde{r}} \bar{u}^{(0)} + \bar{V}_r(r) \partial_{\tilde{r}} \bar{u}^{(0)} - D \left[\partial_{\tilde{r}}^2 \bar{u}^{(0)} + \frac{1}{\bar{r}} \partial_{\tilde{r}} \bar{u}^{(0)} \right] = D \bar{E} \left[\partial_{\tilde{r}}^2 \bar{u}^{(0)} - \frac{1}{\bar{r}} \partial_{\tilde{r}} \bar{u}^{(0)} \right], \quad (\text{A29b})$$

where $\bar{E} = \bar{V}_r^2 \bar{h}^2 / 210 D^2$. Finally, through the nondimensionalization used in Sec. II, Eq. (A29a) transforms into Eq. (10). The equations for the concentrations of B and C can be derived analogously.

When $E(r) = 0$, these equations have the same form as those governing the dynamics for 1D $A + B \rightarrow C$ fronts in polar geometry [29]. We assume that the reaction occurs in a region whose width, in the long-time limit, is much smaller than the depletion zone [15,29,32]. Hence, $u^{(0)}$ varies significantly around $r = r_f$ and it is constant elsewhere. In Sec. IV, we have shown that asymptotically $r_f = r_{f,A} \simeq 2\sqrt{\mathcal{K}t}$. Hence, by substituting this expression into the definition of $E(r)$, we get

$$E(r_f) = \frac{Q^2 h^2}{840 \mathcal{K} t} \ll 1, \quad \text{for } t \gg t_{Ta} = \frac{Q^2 h^2}{840 \mathcal{K}}. \quad (\text{A30})$$

APPENDIX B: COMPARISON OF $R = \langle a \rangle \langle b \rangle$ AND $\tilde{R} = \langle ab \rangle$

In this Appendix, we show that $R \geq \tilde{R}$ pointwise. To do so, we assume that $a(r, z, t)$ and $b(r, z, t)$ are decreasing and

increasing functions of z , respectively, i.e., $\partial_z a \leq 0$ and $\partial_z b \geq 0$ for $0 \leq z \leq h/2$. Figure 15 shows that this assumption is true for different times and distances from the inlet.

By using the definitions of R and \tilde{R} , we obtain

$$R(r, t) = \frac{1}{h^2} \int_{-h/2}^{h/2} a(r, z, t) dz \int_{-h/2}^{h/2} b(r, z, t) dz, \quad (\text{B1a})$$

$$\tilde{R}(r, t) = \frac{1}{h} \int_{-h/2}^{h/2} a(r, z, t) b(r, z, t) dz. \quad (\text{B1b})$$

We perform the change of variables $\zeta = z/h$ and we use the symmetry of the system with respect to $\zeta = 0$. Thus, Eq. (B1) reduce to

$$R(r, t) = 4 \int_0^{1/2} a(r, \zeta, t) d\zeta \int_0^{1/2} b(r, \zeta, t) d\zeta, \quad (\text{B2a})$$

$$\tilde{R}(r, t) = 2 \int_0^{1/2} a(r, \zeta, t) b(r, \zeta, t) d\zeta. \quad (\text{B2b})$$

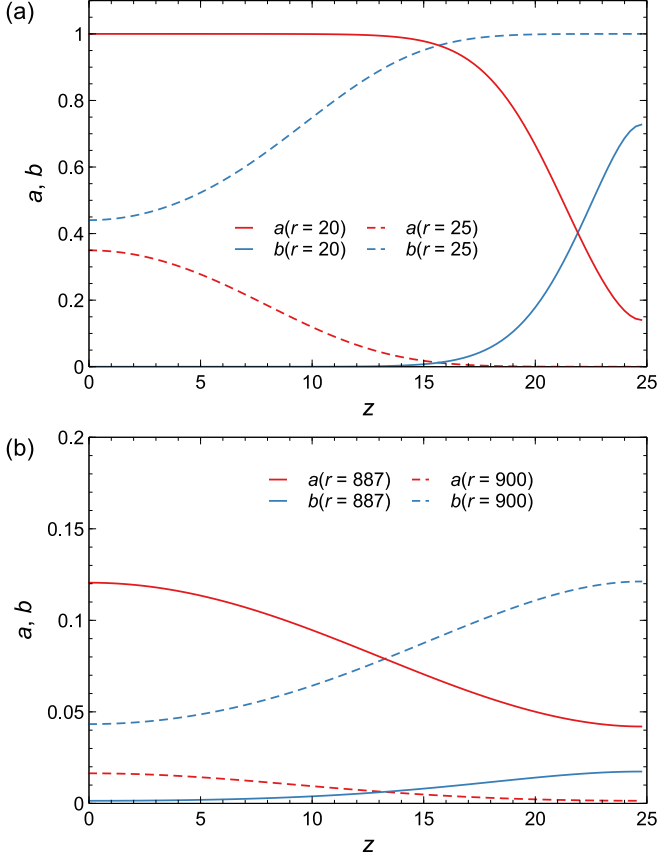


FIG. 15. Concentration profiles along $z \in [0, h/2]$ for $Q = 100$, $h = 50$, and $\gamma = 1$ at (a) $t = 1$ and (b) $t = 4000$.

We introduce the functions $f_1 = a$ and $f_2 = b_m - b$, where $b_m = b(r, \zeta = 1/2, t)$ is the maximum value of b for fixed r and t . Both f_1 and f_2 are thus decreasing functions of ζ . Therefore, we can apply the Chebyshev inequality for integrals ([46], p. 1065)

$$\int_{x_1}^{x_2} f_1(x) dx \int_{x_1}^{x_2} f_2(x) dx \cdots \int_{x_1}^{x_2} f_n(x) dx \leq (x_2 - x_1)^{n-1} \int_{x_1}^{x_2} f_1(x) f_2(x) \cdots f_n(x) dx, \quad (\text{B3})$$

where we set $x_1 = 0$, $x_2 = 1/2$, and $n = 2$. Thus, we obtain

$$\int_0^{1/2} a(r, \zeta, t) d\zeta \int_0^{1/2} [b_m(r, t) - b(r, \zeta, t)] d\zeta \leq \frac{1}{2} \int_0^{1/2} a(r, \zeta, t) [b_m(r, t) - b(r, \zeta, t)] d\zeta, \quad (\text{B4})$$

which implies

$$\int_0^{1/2} a(r, \zeta, t) d\zeta \int_0^{1/2} b(r, \zeta, t) d\zeta \geq \frac{1}{2} \int_0^{1/2} a(r, \zeta, t) b(r, \zeta, t) d\zeta, \quad (\text{B5})$$

and, by using Eq. (B2), we finally get $R(r, t) \geq \tilde{R}(r, t)$.

APPENDIX C: WIDTH OF $d\langle u \rangle/dr$

By subtracting Eq. (10b) from Eq. (10a), we obtain the long-time expression for the average over z of u ,

$$\partial_t \langle u \rangle + \frac{Q-1}{r} \partial_r \langle u \rangle - \partial_r^2 \langle u \rangle = E(r) \left[\partial_r^2 \langle u \rangle - \frac{\partial_r \langle u \rangle}{r} \right], \quad (\text{C1})$$

where

$$E(r) = \frac{Q^2 h^2}{210 r^2}. \quad (\text{C2})$$

To simplify the notation, in the following we will drop the angular brackets and we will write u instead of $\langle u \rangle$. We introduce the change of variables $\xi = [r - r_f(t)]/t^\alpha$ for $\alpha > 0$. Notice that the temporal and radial derivatives of ξ read

$$\frac{\partial \xi}{\partial t} = -\frac{1}{t^\alpha} \frac{dr_f}{dt} - \frac{\alpha \xi}{t} = -\frac{2\mathcal{K}}{t^\alpha r_f} - \frac{\alpha \xi}{t}, \quad (\text{C3a})$$

$$\frac{\partial \xi}{\partial r} = t^{-\alpha}, \quad (\text{C3b})$$

where we have used the asymptotic limit (11) for r_f . Thus, by using this change of variables in Eq. (C1), we get

$$\left[1 + E(r_f + \xi t^\alpha) \right] \frac{d^2 u}{d\xi^2} + \left[\frac{t^\alpha}{r_f + \xi t^\alpha} + \alpha \xi t^{2\alpha-1} + \frac{2\mathcal{K} t^\alpha}{r_f} - \frac{[Q + E(r_f + \xi t^\alpha)] t^\alpha}{r_f + \xi t^\alpha} \right] \frac{du}{d\xi} = 0. \quad (\text{C4})$$

We consider now the limit $t \rightarrow \infty$ for ξ fixed in order to determine the value of α . If $\alpha < 1/2$, the coefficient of $du/d\xi$ vanishes for $t \rightarrow \infty$ because $r_f \sim t^{1/2}$, which would lead to $d^2 u/d\xi^2 = 0$, which does not admit physical solutions. On the other hand, if $\alpha > 1/2$ the coefficient of $du/d\xi$ diverges for $t \rightarrow \infty$, leading to $du/d\xi = 0$, which also does not admit physical solutions. Therefore, $\alpha = 1/2$ and Eq. (C4) reads

$$\left[1 + E(r_f + \xi \sqrt{t}) \right] \frac{d^2 u}{d\xi^2} + \left[\frac{\xi}{2} + \frac{\sqrt{t}}{r_f + \xi \sqrt{t}} + \frac{2\mathcal{K} \sqrt{t}}{r_f} - \frac{[Q + E(r_f + \xi \sqrt{t})] \sqrt{t}}{r_f + \xi \sqrt{t}} \right] \frac{du}{d\xi} = 0. \quad (\text{C5})$$

The derivatives of u are nonzero only near $r = r_f$, so ξ cannot assume large values. Therefore, we write

$$r_f + \xi \sqrt{t} = r_f (1 + \chi), \quad \chi = \frac{\xi}{2\sqrt{\mathcal{K}}}, \quad (\text{C6})$$

where $\chi \ll 1$ if $Q \gg 1$ since $\mathcal{K} \sim Q/2$ and we expand to the first order in χ to get

$$\left[1 + \frac{Q^2 h^2}{210 r_f^2} \left(1 - \frac{2\xi \sqrt{t}}{r_f} \right) \right] d_\xi^2 u + \left[\frac{\xi}{2} + \frac{\sqrt{t}}{r_f} \left(1 - \frac{\xi \sqrt{t}}{r_f} \right) - \frac{Q \sqrt{t}}{r_f} \left(1 - \frac{\xi \sqrt{t}}{r_f} \right) - \frac{Q^2 h^2 \sqrt{t}}{210 r_f^3} \left(1 - \frac{3\xi \sqrt{t}}{r_f} \right) + \frac{2\mathcal{K} \sqrt{t}}{r_f} \right] d_\xi u = 0. \quad (\text{C7})$$

Rearranging the terms and using Eq. (11), we obtain

$$\left[1 + \frac{Q^2 h^2}{840\mathcal{K}t} - \frac{Q^2 h^2 \xi}{840\mathcal{K}^{3/2}t}\right] d_\xi^2 u + \left[\xi \left(\frac{1}{2} + \frac{Q-1}{4\mathcal{K}}\right) + \frac{Q^2 h^2}{1120\mathcal{K}^2 t}\right] d_\xi u + \left[\frac{1-Q+2\mathcal{K}}{2\sqrt{\mathcal{K}}} - \frac{Q^2 h^2}{1680\mathcal{K}^{3/2}t}\right] d_\xi u = 0. \quad (\text{C8})$$

We recall that the equation for u is only valid in the long-time limit, which is defined by the timescale (A30). Therefore, we define $t = \bar{t} t_{TA}$ where $\bar{t} \gtrsim 1$. By performing this change of variable in Eq. (C8), we obtain

$$\left[1 + \bar{t}^{-1} \left(1 - \frac{1}{\sqrt{\mathcal{K}}}\right)\right] d_\xi^2 u + \left[\xi \left(\frac{1}{2} + \frac{Q-1}{4\mathcal{K}} + \frac{3}{4\mathcal{K}\bar{t}}\right) + \frac{1-Q+2\mathcal{K}}{2\sqrt{\mathcal{K}}} - \frac{1}{2\sqrt{\mathcal{K}\bar{t}}}\right] d_\xi u = 0. \quad (\text{C9})$$

Recalling that $\mathcal{K} \simeq Q/2$ for $Q \gg 1$ and $\gamma \simeq 1$ and that \bar{t} is of order one, by keeping the first correction only, we get

$$A(\bar{t}) d_\xi^2 u + \xi d_\xi u = 0, \quad (\text{C10})$$

where $A(\bar{t}) = 1 + \bar{t}^{-1}$ and the boundary conditions are $u(-\infty) = 1$ and $u(\infty) = -\gamma$. The solution of Eq. (C10) thus reads (we now restore the angular brackets)

$$\langle u(\xi) \rangle = \frac{1-\gamma}{2} - \frac{1+\gamma}{2} \operatorname{erf}\left(\frac{\xi}{\sqrt{2A(\bar{t})}}\right). \quad (\text{C11})$$

By replacing $\bar{t} = t/t_{TA}$ into the expression of $A(\bar{t})$, we obtain

$$A(t) = 1 + \frac{Qh^2}{420t}, \quad (\text{C12})$$

where we use $\mathcal{K} = Q/2$. However, as shown in Fig. 16(a), a nice agreement between Eq. (C11) and the numerical solution of Eq. (C1) is obtained provided that we use

$$A(t) = 1 + \frac{Qh^2}{210t}. \quad (\text{C13})$$

We do not have an explanation for this incorrect factor 2. We will thus use Eq. (C13) in the following.

We consider now the radial gradient of $\partial_r \langle u \rangle$ and its width w_u defined as the second centered moment of $\partial_r \langle u \rangle$,

$$\begin{aligned} w_u^2(t) &= \frac{\int_0^\infty [r - r_f(t)]^2 \partial_r \langle u \rangle dr}{\int_0^\infty \partial_r \langle u \rangle dr} \\ &= -\frac{1}{1+\gamma} \int_0^\infty [r - r_f(t)]^2 \partial_r \langle u \rangle dr. \end{aligned} \quad (\text{C14})$$

We use again the change of variable $\xi = (r - r_f)/\sqrt{t}$, which reduces Eq. (C14) to

$$w_u^2(t) = -\frac{t}{1+\gamma} \int_0^\infty \xi^2 d_\xi \langle u \rangle d\xi, \quad (\text{C15})$$

where we can approximate the integral as performed over all the real domain since du/dr is a well-peaked function around $\xi = 0$. The derivative of (C11) reads

$$\frac{d\langle u \rangle}{d\xi} = -\frac{1+\gamma}{2} \sqrt{\frac{2}{\pi A}} \exp(-\xi^2/2A). \quad (\text{C16})$$

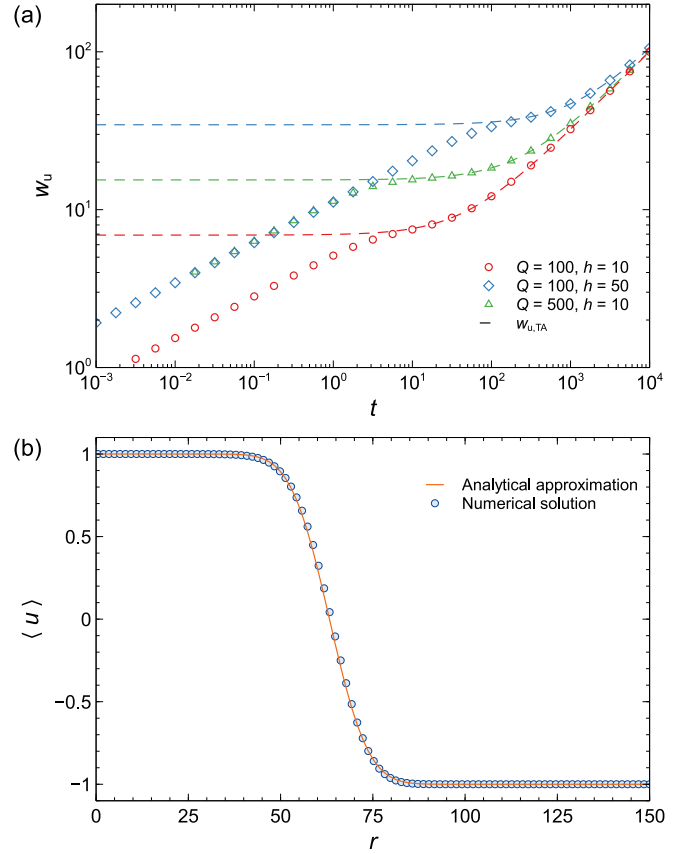


FIG. 16. (a) Temporal evolution of w_u . Results for $\gamma = 1$. The dashed lines indicate Eq. (C17). (b) Comparison between the numerical solution of Eq. (C1) and the analytical approximation (C11) for $Q = 100$, $h = 10$, $\gamma = 1$ at $t = 20$.

By substituting this expression into Eq. (C15), we finally obtain the long-time expression for the width $w_{u,TA}$ of $|d\langle u \rangle/dr|$,

$$w_{u,TA} = \sqrt{t + t_c}, \quad t_c = \frac{Qh^2}{210}, \quad (\text{C17})$$

where the index TA stands for transient- and long-time regimes. Figure 16 shows that the obtained expression exhibits good agreement with the numerical results.

APPENDIX D: DERIVATION OF $w_{c,A}$ IN 1D POLAR GEOMETRY

We compute here the width $w_{c,A}$ for the 1D radial system in the limit $t \rightarrow \infty$. The evolution of the product concentration c is governed by the equation [29]

$$\partial_t c(r, t) + \frac{Q-1}{r} \partial_r c(r, t) - \partial_r^2 c(r, t) - R(r, t) = 0, \quad (\text{D1})$$

where $R = ab$ is well peaked around the front position r_f where $a = b$. Thus, we write

$$R(r, t) = R[r_f(t)] f\left(\frac{r - r_f(t)}{w}\right), \quad (\text{D2})$$

where w is the width of R . We assume that in the long-time limit the maximum concentration of C is located at the position where the production rate is maximum, i.e., $r_c \simeq r_f$. For

$Q \gg 1$ and $\gamma \simeq 1$ the long-time front position (11) reads

$$r_{f,A}(t) \simeq \sqrt{2Qt}. \quad (\text{D3})$$

The width of C is defined as

$$w_c(t) = \left[\frac{\int_0^\infty (r - r_c)^2 c(r, t) dr}{\int_0^\infty c(r, t) dr} \right]^{1/2}. \quad (\text{D4})$$

By performing the change of variable $x = r - r_c \simeq r - r_f$, Eq. (D4) reduces to

$$w_c(t) = \left[\frac{\int_{-r_f}^\infty x^2 c(x, t) dx}{\int_{-r_f}^\infty c(x, t) dx} \right]^{1/2}. \quad (\text{D5})$$

Since c is peaked around $x = 0$, we assume that $r_f \gg w_c$ (which, as seen below, is true for $Q \gg 1$), so that, in virtue of Eq. (D3), we can replace the lower limit of integration $-r_f$ in Eq. (D5) by $-\infty$. Hence, Eq. (D5) reads

$$w_{c,A}(t) = \left[\frac{\int_{-\infty}^\infty x^2 c(x, t) dx}{\int_{-\infty}^\infty c(x, t) dx} \right]^{1/2}. \quad (\text{D6})$$

By adopting the same change of variables, Eq. (D1) reads

$$\partial_t c(x, t) + \frac{Q-1}{x+r_f(t)} \partial_x c(x, t) - \partial_x^2 c(x, t) - R(x, t) = 0. \quad (\text{D7})$$

Because we have assumed $w_c \ll r_f$, the term $(x+r_f)^{-1} \ll 1$ when $t \rightarrow \infty$. Hence, in this long-time limit Eq. (D7) reduces to

$$\partial_t c(x, t) - \partial_x^2 c(x, t) - R(x, t) = 0. \quad (\text{D8})$$

Integrating this equation over x leads to

$$\int_{-\infty}^\infty \partial_t c(x, t) dx = \int_{-\infty}^\infty R(x, t) dx, \quad (\text{D9})$$

where we used $\int_{-\infty}^\infty \partial_x^2 c dx = 0$, since $\partial_x c = 0$ for $|x| \gg w_c$. By substituting Eq. (D2) into Eq. (D9), we get

$$\partial_t \int_{-\infty}^\infty c(x, t) dx = \alpha R[r_f(t)] w(t), \quad (\text{D10})$$

where $\alpha = \int_{-\infty}^\infty f(x) dx$. In the long-time limit $R(r_f) \rightarrow R_A^{\max}$ and $w \rightarrow w_A$, which are given as in Eqs. (13) and (14), respectively. Hence, by integrating Eq. (D10) in time, we obtain

$$\int_{-\infty}^\infty c(x, t) dx = \frac{58\alpha}{\pi^3} K t^{1/2}, \quad (\text{D11})$$

which provides the denominator in Eq. (D6). To obtain an expression for the numerator, we first multiply Eq. (D8) by x^2 and then we integrate over x to obtain

$$\int_{-\infty}^\infty x^2 \partial_t c(x, t) dx = \int_{-\infty}^\infty x^2 \partial_x^2 c(x, t) dx + \int_{-\infty}^\infty x^2 R(x, t) dx. \quad (\text{D12})$$

By integrating twice by parts the term $\int_{-\infty}^\infty x^2 \partial_x^2 c dx$ and by recalling that c and $\partial_x c$ vanish for $|x| \rightarrow \infty$, we obtain

$$\int_{-\infty}^\infty x^2 \partial_x^2 c(x, t) dx = 2 \int_{-\infty}^\infty c(x, t) dx = \frac{116\alpha}{\pi^3} K t^{1/2}, \quad (\text{D13})$$

where we have used Eq. (D11). Furthermore, by using Eq. (D2), we get

$$\int_{-\infty}^\infty x^2 R(x, t) dx = \beta R[r_f(t)] w^3(t), \quad (\text{D14})$$

where $\beta = \int_{-\infty}^\infty x^2 f(x) dx$. By substituting Eqs. (13) and (14) into Eq. (D14), we obtain

$$\int_{-\infty}^\infty x^2 R(x, t) dx = \frac{29\beta}{\pi} K^{1/3} t^{-1/6}, \quad (\text{D15})$$

which vanishes for $t \rightarrow \infty$. Hence, by substituting Eq. (D13) into Eq. (D12) and by neglecting the term of Eq. (D15), we get

$$\partial_t \int_{-\infty}^\infty x^2 c(x, t) dx = \frac{116\alpha}{\pi^3} K t^{1/2}. \quad (\text{D16})$$

Time integration finally provides

$$\int_{-\infty}^\infty x^2 c(x, t) dx = \frac{232\alpha}{3\pi^3} K t^{3/2}. \quad (\text{D17})$$

By substituting Eqs. (D17) and (D11) into Eq. (D6) we obtain

$$w_{c,A}(t) = \sqrt{\frac{4}{3}t}. \quad (\text{D18})$$

In dimensional units, Eq. (D18) reads

$$\tilde{w}_{c,A}(\tilde{t}) = \sqrt{\frac{4}{3}D\tilde{t}}. \quad (\text{D19})$$

APPENDIX E: EARLY-TIME ANALYSIS

The early-time analysis is performed by assuming that in this regime the amount of mixing between the reactants is small and that transverse diffusion is negligible. As a consequence of these assumptions, the reaction terms ab and the derivative along z that appear in Eq. (3a) can be neglected. Therefore, we approximate Eq. (3a) in the early-time regime as

$$\partial_t a_E + \frac{\tilde{Q}(z) - 1}{r} \partial_r a_E = \partial_r^2 a_E, \quad (\text{E1a})$$

$$\partial_t b_E + \frac{\tilde{Q}(z) - 1}{r} \partial_r b_E = \partial_r^2 b_E, \quad (\text{E1b})$$

where $a_E(r, z, t)$ and $b_E(r, z, t)$ denote the early-time dimensionless concentration of the reactants A and B , respectively, and

$$\tilde{Q}(z) = \frac{3}{2} \left(1 - \frac{4z^2}{h^2} \right) Q. \quad (\text{E2})$$

Notice that this equation is similar to the equation for the conservative component $u = a - b$ in the 1D polar case [29]. In fact, because diffusion along z is neglected, there is no mechanism that couples the equations in r and z , so that

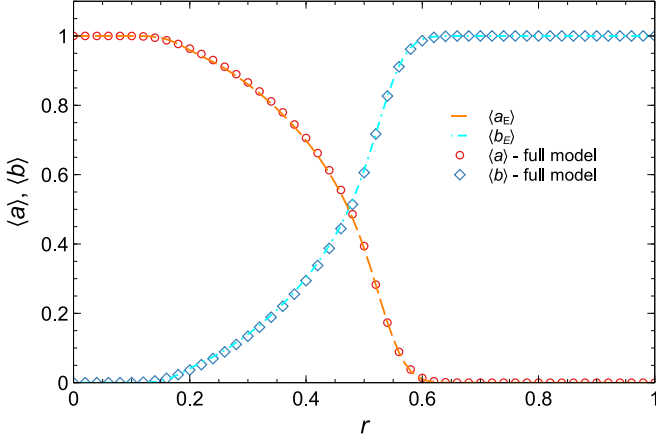


FIG. 17. Radial profiles of $\langle a \rangle$ and $\langle b \rangle$ for $Q = 100$, $h = 20$, and $\gamma = 1$ at $t = 10^{-3}$. The symbols indicate the results obtained by solving numerically Eq. (3), while the lines represent Eqs. (E6) and (E7).

Eq. (E1a) describes a set of independent equations for any given value of z in $[-h/2, h/2]$. These equations are solved by introducing the change of variables $\eta = r^2/4t$, which allows us to transform the PDE (E1a) into the ODE

$$\partial_\eta^2 a_E + \left(1 + \frac{1 - \tilde{Q}(z)/2}{\eta}\right) \partial_\eta a_E = 0. \quad (\text{E3})$$

The general solution reads

$$a_E(r, z, t) = c_1 + c_2 \Gamma\left(\frac{\tilde{Q}(z)}{2}, \frac{r^2}{4t}\right), \quad (\text{E4})$$

where c_1 and c_2 are integration constants that are determined by applying the boundary conditions $a_E(0, z, t) = 1$ and $a_E(r \rightarrow \infty, z, t) = 0$, so that

$$a_E(r, z, t) = Q\left(\frac{\tilde{Q}(z)}{2}, \frac{r^2}{4t}\right), \quad (\text{E5})$$

where Q is the regularized gamma function. The average concentration is obtained by calculating the integral along the gap numerically,

$$\langle a_E \rangle = \frac{1}{h} \int_{-h/2}^{h/2} Q\left(\frac{\tilde{Q}(z)}{2}, \frac{r^2}{4t}\right) dz. \quad (\text{E6})$$

One can obtain the equation for the early-time concentration b_E of B analogously. Because the reaction term is neglected, notice that we must have $b_E = \gamma(1 - a_E)$ and in particular

$$\langle b_E \rangle = \gamma(1 - \langle a_E \rangle). \quad (\text{E7})$$

Figure 17 shows that the calculated averaged concentrations in Eq. (E6) and Eq. (E7) are in good agreement with the numerical solutions of Eq. (3).

By using Eq. (E7), the early-time production rate $R_E = \langle a_E \rangle \langle b_E \rangle$ reads

$$R_E(r, t) = \gamma \langle a_E \rangle (1 - \langle a_E \rangle). \quad (\text{E8})$$

Notice that the maximum R_E^{\max} along r is found for $\langle a_E \rangle = \langle b_E \rangle = 1/2$ and its value is $R_E^{\max} = \gamma/4$. To obtain the front position r_E^{\max} as the distance from the inlet at which R_E is

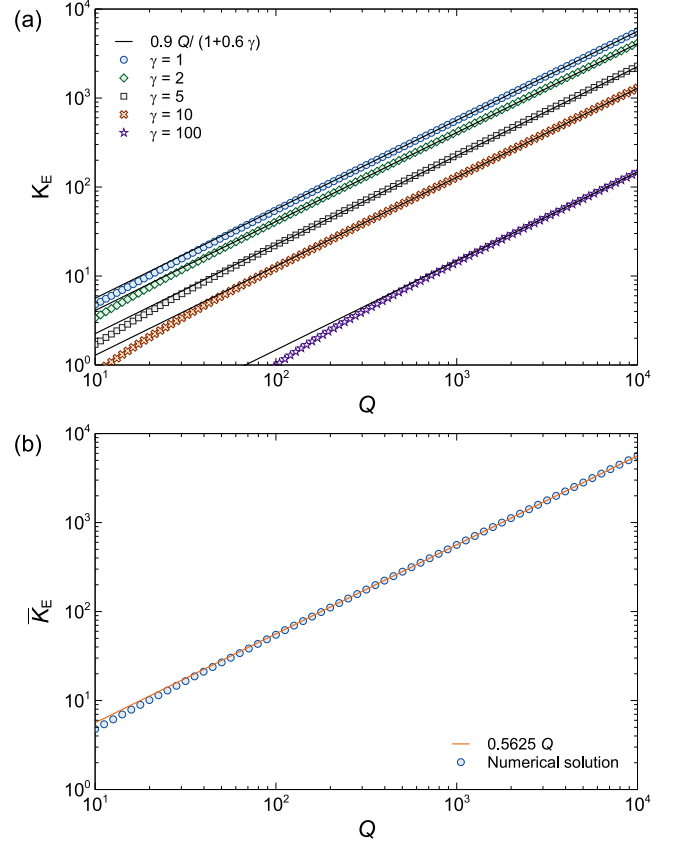


FIG. 18. (a) Comparison between the approximated expression (21b) and numerical results. (b) Comparison between \bar{K}_E = $0.5625 Q$ and the numerical results.

maximum, we set $\langle a_E \rangle = 1/2$ in Eq. (E6),

$$\int_0^{h/2} Q\left(\frac{\tilde{Q}(z)}{2}, \frac{r^2}{4t}\right) dz = \frac{h}{4}, \quad (\text{E9})$$

where we have used the symmetry of the system along the z axis. Through the changes of variable $y = 1 - 4z^2/h^2$ and $\eta = r^2/4t$, and by using Eq. (E2), we obtain

$$f(Q, \eta) = 1, \quad f(Q, \eta) = \int_0^1 \frac{Q\left(\frac{3Qy}{4}, \eta\right) dy}{\sqrt{1-y}}. \quad (\text{E10})$$

The solution $\eta = \bar{K}_E(Q)$ is found by solving Eq. (E10) numerically. We find $\bar{K}_E \simeq 0.5625 Q$; see Fig. 18(b). Hence, the position of the maximum of the production rate at early-time reads

$$r_E^{\max} = 2\sqrt{\bar{K}_E(Q)t} = \sqrt{2.25 Q t}. \quad (\text{E11})$$

The front position $r_{f,E}$, defined as the location where $\langle a_E \rangle = \langle b_E \rangle$, is obtained in a similar way. Equation (E7) here gives $\langle a_E \rangle = \gamma/(1 + \gamma)$, which we substitute into Eq. (E6) and get

$$\int_0^{h/2} Q\left(\frac{\tilde{Q}(z)}{2}, \frac{r^2}{4t}\right) dz = \frac{h}{2} \left(\frac{\gamma}{1 + \gamma}\right). \quad (\text{E12})$$

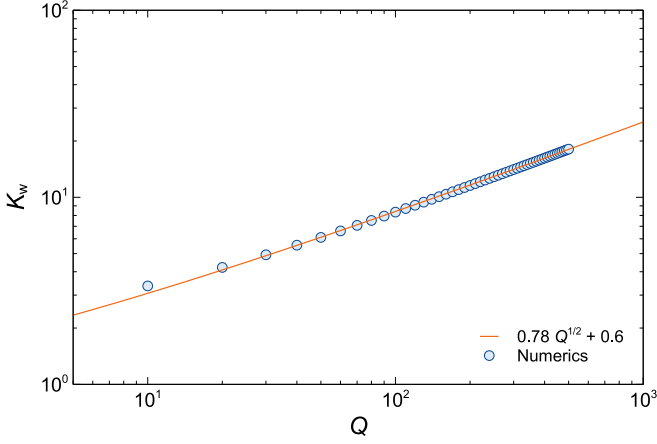


FIG. 19. Comparison of the approximated K_w and the results of numerical computations.

By using the previous changes of variables and by using the definition (E10) of $f(Q, \eta)$ the latter reduces to

$$f(Q, \eta) = \frac{2\gamma}{1 + \gamma}. \quad (\text{E13})$$

We find numerically the solution $\eta = 0.9Q/(1 + 0.6\gamma)$, and by substituting the definition of η , we finally obtain Eq. (21a). Figure 18 shows the comparison between the coefficients K_E , given by Eq. (21b), and \bar{K}_E , given above, computed numerically and their analytical approximations.

To compute the front width w_E as the width at half height of $R_E = \langle a_E \rangle \langle b_E \rangle$, we notice that the values of $\langle a_E \rangle$ for which $R_E = R_E^{\max}/2 = \gamma/8$ are

$$\langle a_E^{\pm} \rangle = \frac{1}{2}(1 \pm \sqrt{2}/2). \quad (\text{E14})$$

Substituting this into Eq. (E6), we obtain

$$\frac{1}{2} \left(1 \pm \frac{\sqrt{2}}{2} \right) = \frac{1}{h} \int_{-h/2}^{h/2} \mathcal{Q} \left(\frac{\tilde{Q}(z)}{2}, \frac{r^2}{4t} \right) dz. \quad (\text{E15})$$

Repeating the steps that we took to calculate r_E^{\max} we obtain the equation

$$f(Q, \eta) = 1 \pm \sqrt{2}/2, \quad (\text{E16})$$

where $f(Q, \eta)$ is defined by Eq. (E10). The solutions $\eta_{\pm} = r_{\pm}^2/4t$ are computed numerically as a function of Q (see Fig. 19). The width w_E is finally expressed as

$$w_E(t) = r_+(t) - r_-(t) = K_w(Q)t^{1/2}, \quad (\text{E17})$$

where $K_w = 2(\sqrt{\eta_+} - \sqrt{\eta_-}) \simeq 0.78Q^{1/2}$. Recalling that in the early-time regime, Eq. (E1a) describes a set of independent equations for each value of z , we compute the total amount of product $n_{c,E}$ as

$$n_{c,E} = \int_{-h/2}^{h/2} n_{c,E}^{(1D)}(z) dz, \quad (\text{E18})$$

where $n_{c,E}^{(1D)}(z, t) = 2\pi \int_0^{\infty} rc(r, z, t) dr$ is the total amount of product along a streamline, obtained from Eq. (E1). By using

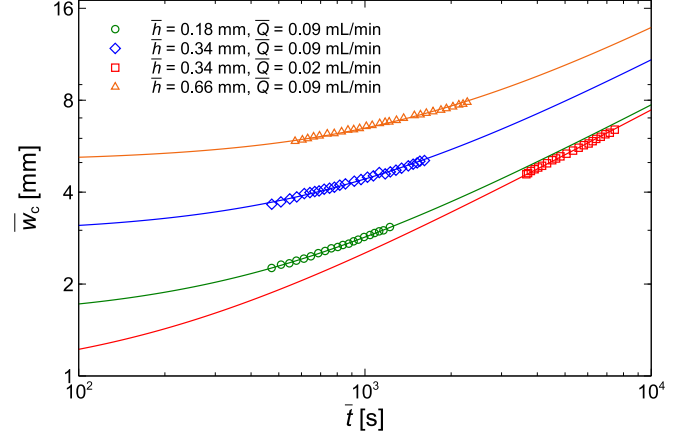


FIG. 20. Temporal evolution of \bar{w}_c from the experimental work [33]. The solid lines represent the theoretical predictions (16), where c_γ and D are obtained through fitting.

the relationship [29]

$$\frac{dn_{c,E}^{(1D)}}{dt} = 2\pi \int_0^{\infty} r R_E(r, z, t) dr, \quad (\text{E19})$$

where $R_E(r, z, t) = a_E(r, z, t)b_E(r, z, t)$, and Eq. (E5) together with $b_E = \gamma(1 - a_E)$, we obtain

$$\frac{dn_{c,E}^{(1D)}}{dt} = 2\pi\gamma \int_0^{\infty} r \mathcal{Q} \left(\frac{\tilde{Q}}{2}, \frac{r^2}{4t} \right) \left[1 - \mathcal{Q} \left(\frac{\tilde{Q}}{2}, \frac{r^2}{4t} \right) \right] dr. \quad (\text{E20})$$

Performing the integral, we get

$$\frac{dn_{c,E}^{(1D)}}{dt} = 4\sqrt{\pi}\gamma \frac{\Gamma(\frac{1+\tilde{Q}}{2})}{\Gamma(\frac{\tilde{Q}}{2})} t. \quad (\text{E21})$$

Time integration leads to

$$n_{c,E}^{(1D)}(z, t) \simeq \sqrt{2\pi}\gamma \tilde{Q}^{1/2}(z)t^2, \quad (\text{E22})$$

where we used the approximation $\Gamma[(1 + \tilde{Q})/2]/\Gamma(\tilde{Q}/2) \simeq \sqrt{\tilde{Q}/2}$ for $\tilde{Q} \gg 1$. Finally, by substituting Eq. (E22) and Eq. (E2) into Eq. (E18) and by computing the integral along the gap we get

$$n_{c,E}(t) \simeq \frac{\sqrt{3\pi^3}}{4} \gamma h Q^{1/2} t^2. \quad (\text{E23})$$

APPENDIX F: COMPARISON WITH EXPERIMENTAL RESULTS

In this Appendix, we compare our model to the experimental results in Ref. [33]. Specifically, we focus on the width \bar{w}_c of the product concentration, which is shown in Fig. 20. In our model, the transient- and long-time behavior of this quantity is described in dimensional units by Eq. (16). The multiplicative coefficient c_γ and the diffusion coefficient are used as fitting parameters. We find $D = (8.2 \pm 0.7) \times 10^{-10} \text{ m}^2/\text{s}$, which is of the expected magnitude. Since the reactants are in equal concentrations, Eq. (15b) predicts $c_\gamma = 1.23$, while from

fitting we obtain values in the range 2.2–3.9. Such a difference could be motivated by effects that are not accounted for in this

model, including, e.g., buoyancy, premixing in the injection tube, or the finite radius of the injection valve.

-
- [1] J. D. Murray, *Mathematical Biology* (Springer, Berlin, 2003).
- [2] J. V. Noble, *Nature (London)* **250**, 726 (1974).
- [3] R. M. Anderson and R. M. May, *Infectious Diseases of Humans: Dynamics and Control* (Oxford University Press, Oxford, 1992).
- [4] V. Belik, T. Geisel, and D. Brockmann, *Phys. Rev. X* **1**, 011001 (2011).
- [5] S. Kondo and T. Miura, *Science* **329**, 1616 (2010).
- [6] A. Tóth, I. Lagzi, and D. Horváth, *J. Phys. Chem.* **100**, 14837 (1996).
- [7] U. Ebert and W. van Saarloos, *Physica D (Amsterdam)* **146**, 1 (2000).
- [8] F. A. Williams, *Combustion Theory* (CRC Press, Boca Raton, 1994).
- [9] I. Mastromatteo, B. Toth, and J.-P. Bouchaud, *Phys. Rev. Lett.* **113**, 268701 (2014).
- [10] P. J. Ortoleva, *Geochemical Self-Organization* (Oxford University Press, Oxford, 1994).
- [11] B. Heidel, C. M. Knobler, R. Hilfer, and R. Bruinsma, *Phys. Rev. Lett.* **60**, 2492 (1988).
- [12] J. H. Seinfeld and S. N. Pandis, *Atmospheric Chemistry and Physics*, 2nd ed. (John Wiley and Sons, New York, 2006).
- [13] A. Okubo and S. A. Levin, *Diffusion and Ecological Problems: Modern Perspectives* (Springer Science and Business Media, 2013).
- [14] E. R. Abraham, *Nature (London)* **391**, 577 (1998).
- [15] L. Gálfi and Z. Rácz, *Phys. Rev. A* **38**, 3151 (1988).
- [16] Z. Jiang and C. Ebner, *Phys. Rev. A* **42**, 7483 (1990).
- [17] Y.-E. L. Koo and R. Kopelman, *J. Stat. Phys.* **65**, 893 (1991).
- [18] S. H. Park, S. Parus, R. Kopelman, and H. Taitelbaum, *Phys. Rev. E* **64**, 055102(R) (2001).
- [19] D. Brockmann and D. Helbing, *Science* **342**, 1337 (2013).
- [20] K. Tsuji and S. C. Müller, *J. Phys. Chem. Lett.* **3**, 977 (2012).
- [21] M. Dayeh, M. Ammar, and M. Al-Ghoul, *RSC Adv.* **4**, 60034 (2014).
- [22] M. Al-Ghoul and R. Sultan, *Phys. Rev. E* **100**, 052214 (2019).
- [23] G. Schuszter, F. Brau, and A. De Wit, *Environ. Sci. Technol. Lett.* **3**, 156 (2016).
- [24] F. Haudin, J. H. E. Cartwright, F. Brau, and A. De Wit, *Proc. Natl. Acad. Sci. USA* **111**, 17363 (2014).
- [25] B. Bohner, G. Schuszter, O. Berkesi, D. Horváth, and Á. Tóth, *Chem. Commun.* **50**, 4289 (2014).
- [26] V. Sebastian, S. A. Khan, and A. Kulkarni, *J. Flow Chem.* **7**, 96 (2017).
- [27] I. Ziemecka, S. Gokalp, S. Stroobants, F. Brau, D. Maes, and A. De Wit, *Crystals* **9**, 351 (2019).
- [28] B. M. Shipilevsky, *Phys. Rev. E* **95**, 062137 (2017).
- [29] F. Brau, G. Schuszter, and A. De Wit, *Phys. Rev. Lett.* **118**, 134101 (2017).
- [30] F. Brau and A. De Wit, *J. Chem. Phys.* **152**, 054716 (2020).
- [31] P. M. J. Trevelyan and A. J. Walker, *Phys. Rev. E* **98**, 032118 (2018).
- [32] A. Comolli, A. De Wit, and F. Brau, *Phys. Rev. E* **100**, 052213 (2019).
- [33] A. Tóth, G. Schuszter, N. P. Das, E. Lantos, D. Horváth, A. De Wit, and F. Brau, *Phys. Chem. Chem. Phys.* **22**, 10278 (2020).
- [34] V. Kapoor, C. T. Jafvert, and D. A. Lyn, *Water Resour. Res.* **34**, 1997 (1998).
- [35] E. Guilbert, Une réaction chimique pour le mélange, Ph.D. thesis, Université Aix-Marseille, 2020.
- [36] G. M. Porta, J.-F. Thovert, M. Riva, A. Guadagnini, and P. M. Adler, *Phys. Rev. E* **86**, 036102 (2012).
- [37] D. A. Benson, S. Pankavich, and D. Bolster, *Adv. Water Resour.* **123**, 40 (2019).
- [38] L. J. Perez, J. J. Hidalgo, and M. Dentz, *Water Resour. Res.* **55**, 249 (2019).
- [39] J. Jackson and G. Symmons, *Appl. Sci. Res.* **15**, 59 (1966).
- [40] S. Wilson, *Appl. Sci. Res.* **25**, 349 (1972).
- [41] G. I. Taylor, *Proc. R. Soc. London A* **219**, 186 (1953).
- [42] M. Shapiro and H. Brenner, *AIChE J.* **33**, 1155 (1987).
- [43] H. Taitelbaum, S. Havlin, J. E. Kiefer, B. Trus, and G. H. Weiss, *J. Stat. Phys.* **65**, 873 (1991).
- [44] F. W. J. Olver, D. W. Lozier, R. F. Boisvert, and C. W. Clark, *NIST Handbook of Mathematical Functions* (Cambridge University Press, Cambridge, 2010).
- [45] H. Taitelbaum, Y.-E. L. Koo, S. Havlin, R. Kopelman, and G. H. Weiss, *Phys. Rev. A* **46**, 2151 (1992).
- [46] I. S. Gradshteyn and I. M. Ryzhik, *Table of Integrals, Series, and Products* (Academic Press, Burlington, 2007).